Research Square

Preprints are preliminary reports that have not undergone peer review.
They should not be considered conclusive, used to inform clinical practice,
or referenced by the media as validated information.

# The connectivity-mass relation of eRASS1 galaxy clusters

**Nicola Malavasi**

malavasi@mpe.mpg.de

Max Planck Institute for Extraterrestrial Physics https://orcid.org/0000-0001-9033-7958

**Esra Bulbul**

Max Planck Institute for Extraterrestrial Physics

**Matthias Kluge**

Max Planck Institute for Extraterrestrial Physics

**Xiaoyuan Zhang**

Max Planck Institute for Extraterrestrial Physics https://orcid.org/0000-0001-6019-6373

**Emmanuel Artis**

Max Planck Institute for Extraterrestrial Physics

**Fabian Balzer**

Max Planck Institute for Extraterrestrial Physics

**Nicolas Clerc**

IRAP, Université de Toulouse, CNRS, UPS, CNES

**Johan Comparat**

Université Grenoble Alpes

**Ziyu Ding**

Max Planck Institute for Extraterrestrial Physics https://orcid.org/0009-0006-5863-0648

**Klaus Dolag**

USM LMU; Max Planck Institute for Astrophysics, Garching

**Luca Fiorino**

Max Planck Institue for Extraterrestrial Physics https://orcid.org/0009-0008-8885-6909

**Vittorio Ghirardini**

INAF, Osservatorio di Astrofisica e Scienza dello Spazio

**Sebastian Grandis**

Universität Innsbruck, Institut für Astro- und Teilchenphysik

**Andrea Merloni**

Max Planck Institute for Extraterrestrial Physics https://orcid.org/0000-0002-0761-0130

**Tobias Mistele**

Max Planck Institue for Extraterrestrial Physics

**Kirpal Nandra**

Max-Planck-Institut für extraterrestrische Physik https://orcid.org/0000-0002-7150-9192
**Miriam Ramos-Ceja**
Max Planck Institute for Extraterrestrial Physics https://orcid.org/0000-0002-9117-3251
**Jeremy Sanders**
Max Planck Institute for Extraterrestrial Physics https://orcid.org/0000-0003-2189-4501
**Silas Zelmer**
Max Planck Institue for Extraterrestrial Physics

**Article**

**Keywords:**

**Posted Date:** November 24th, 2026

**DOI:** https://doi.org/10.21203/rs.3.rs-11221544/v1

**License:** This work is licensed under a Creative Commons Attribution 4.0 International License.
Read Full License

**Additional Declarations:** There is **NO** Competing Interest.

# The connectivity-mass relation of eRASS1 galaxy clusters

**Abstract**

Matter distribution in the Universe is inhomogeneous at scales larger than galaxy clusters. It takes the shape of a vast network of structures called the cosmic web, in which galaxy clusters are located at the nodes and connected by filaments (elongated structures containing galaxies, dark matter and gas). As clusters grow by accreting matter from these filaments, their mass is expected to correlate with the number of filaments connected to them. Observational searches for this connectivity-mass relation have so far been limited by the size of the cluster and filament samples, or have relied on optically selected clusters. Here we present the most comprehensive observational study of the connectivity-mass relation to date, using more than 6700 X-ray selected clusters from the eROSITA All-Sky Survey, covering almost half of the sky, combined with a filament catalog constructed from galaxies with photometric redshift measurements over the same area. For the first time, we detect the connectivity-mass relation at different redshifts. We quantify the systematic effects of the cosmic web extraction process and of the photometric redshift precision on our results. We show that high-quality redshifts are required to recover the the slope of the relation. The slope of the recovered connectivity-mass relation also becomes shallower with the increasing purity of the filament sample. Our analysis establishes a workflow to derive the connectivity-mass relation for a sample of clusters, with an exploration of all the possible systematic effects on this measurement. We also provide a measurement with which to compare future studies of the connectivity-mass relation and provide a reference for testing numerical simulations and cosmological models of the Universe.

**Keywords:** keyword1, Keyword2, Keyword3, Keyword4

## 1 Main

The cosmic web (CW) is the way in which we describe matter distribution in the Universe. It takes the shape of a vast network of structures ([1–9]) made of dark matter, gas, and galaxies. Galaxy clusters occupy the position of nodes in this network and are connected among them by filaments. Filaments are one dimensional structures with a lower density than clusters. Simulations suggest that, throughout their evolution, clusters accrete matter from the filaments of the CW ([10]), predominantly at high

redshift ([11, 12]). In fact, filaments can pierce the virial shock of haloes and funnel cold gas onto the forming structures at the center ([10, 13–17]). We can therefore expect more connected clusters to grow more massive with time. This would result in an expected correlation between cluster mass (or cluster overdensity) and number of connected filaments (connectivity) visible also at low redshift ([18]).

Several works have explored this connectivity-mass relation using observed cluster and filament samples and numerical simulations. For example, [19] used the AMASCFI sample from the Canada-France-Hawaii Legacy Survey (CFHTLS, [20, 21]) to measure the connectivity-mass relation for clusters in the redshift range $0.15 \leq z \leq 0.7$ and at masses $M_{200} \geq 10^{14} M_{\odot}$. Similarly, [22] performed the analysis using the COSMOS2015 sample ([23]) at masses $M_{200} \geq 10^{13.38} M_{\odot}$ and in the redshift range $0.5 \leq z \leq 1.2$. The study of the connectivity-mass relation was the subject of a study ([24]) also in the recent Q1 partial data release of the Euclid survey ([25]). In this case, the redshift range covered was $0.2 \leq z \leq 0.7$ while the samples analyzed contained clusters with masses $M_{500c} \geq 10^{13.5} M_{\odot}$. All these works detected a relation between cluster mass and the number of filaments connected. Instead of investigating statistically significant samples of clusters, [26–31] focused on a single cluster, studying its connections to the filaments of the CW in great detail. From the numerical simulation side, a connectivity-mass relation was recovered for simulated clusters by [19, 22, 32–34].

However, the observational works cited above all present limitations. [19] rely on a cluster sample of 7100 clusters detected using photometric redshifts, the majority of which lacks X-ray confirmation. Although [21] performs a match of the clusters analyzed in [19] with existing catalogs of X-ray detected clusters, these samples are very limited in the number of sources that can be used for X-ray confirmation of optically identified clusters ($\lesssim$ 200 X-ray selected clusters). In the case of [22], the limiting factor is survey area (i.e., the $1.38\,\mathrm{deg}^2$ of the COSMOS field), which limits the size of the statistical sample of clusters that can be used (86 in total). This is also the limiting factor in [24] (219 clusters used).

In this work, we advance beyond the state-of-the-art in terms of the detection of the connectivity-mass relation. We do so to create a solid reference, in terms of one of the most thorough characterizations of this relation from observations. We aim at providing a consistent detection over a large mass and redshift range and over a large sky area of the connectivity of a statistically numerous sample of clusters, securely detected via the X-ray emission of their gaseous phase. To achieve this, we measure the connectivity mass relation for the eRASS1 cluster sample ([35, 36]) detected by the extended Röntgen Survey with an Imaging Telescope Array (eROSITA, [37]) onboard the Spectrum-Röntgen-Gamma mission (SRG, [38]).

Achieving a CW detection that covers the German part of the eROSITA sky is certainly challenging. We employ the filaments extracted with DisPerSE over the sky area of the DESI Legacy Imaging Surveys (DESI LS, [39, 40]). This is a large scale filament extraction on $\sim 19\,400\,\mathrm{deg}^2$ performed with a photometric redshift survey, where the effect of photometric redshift uncertainty on the filament reconstruction is taken into account by performing a Montecarlo extraction of galaxy populations (Malavasi et al., under review). We characterize the effect on the connectivity-mass

relation of the strategy used for the cosmic web extraction and of the parameters used to tune the algorithm for the filament extraction and the matching with the cluster sample. Thanks to a thorough comparison with existing literature we set our results in the context of available galaxy surveys and we discover a strong dependency of the slope of the connectivity-mass relation on the quality of the redshift information used to extract the filaments. We provide the first extraction of the connectivity-mass relation in different redshift bins. We also perform the first extraction and comparison of three different relations: the proper connectivity-mass relation, the multiplicity-mass relation, and the filament connections-mass relation.

## 2 The connectivity-mass, multiplicity-mass, and filament connections-mass relations of eRASS1 clusters

We present the measurement of the connectivity-mass, multiplicity-mass, and filament connections-mass relations for the eRASS1 clusters, with the filaments extracted in the DESI LS using DisPerSE. This measurement is achieved by extracting the filaments with DisPerSE from the galaxy distribution, matching the DisPerSE output to the cluster sample to associate critical points to clusters, and then performing the measurement of connectivity, multiplicity, and filament connections. As there is no consensus yet in the literature about the best method to measure these quantities (nor which quantity is related to mass), we analyze in this work all three and we study their relation to mass as a function of redshift. We present in the main text body the most outstanding result, but we include in the methods section the full analysis. We test two strategies for the cosmic web extraction, two levels of the smoothing of the density field, two persistence thresholds (Section 5.1), two subsamples of the main eRASS1 cluster sample (Section 5.2) and we also compare our results with a measurement performed with filaments extracted using spectroscopic redshifts in the GAMA survey (Section 7). Finally, as stated, we do not focus only on connectivity, but we also compare with multiplicity and filament connections (Section 6.3).

Figure 1 shows the connectivity-mass relation for the eRASS1 "Pure" ($\mathcal{L}_{\rm ext} \geq 6$, Section 5.2) sample, derived with the skeleton extracted in the full survey footprint in the case of no smoothing of the density field prior to filament extraction (hereafter "SD0") with a $2\sigma$ persistence threshold (Section 5.1). We fit the connectivity mass relation with two fitting formulae (Section 6.4): a linear fit between $\kappa$ and $\log(M)$ (hereafter "linear") and a linear fit between $\log(\kappa)$ and $\log(M)$ (hereafter "log-log"). We show in Figure 1 the "linear" fit. This figure shows a shallow, but present relation between cluster mass and connectivity, which is visible up to $z \sim 0.27$. There do not appear to be a strong dependence on the relation slope with redshift, and at $z \geq 0.27$ the slope of the relation becomes too shallow to be consistent with being flat. We consistently obtain similar results whether we use the skeleton extracted in the full survey footprint with a $3\sigma$ persistence threshold (Section 9.2) or the postage stamp skeleton extraction with a $2\sigma$ or $3\sigma$ persistence threshold (Section 9.3). In the case of at $3\sigma$ persistence threshold, both for the full survey and the postage stamp skeleton, we find a slightly shallower slope and a relation consistent with being flat above the

lower redshift threshold of $z \sim 0.25$. We also find consistent result whether we use the "Large" ($\mathcal{L}_{\rm ext} \geq 3$, $P_{\rm cont} \leq 0.8$) cluster sample (Section 5.2) instead of the "Pure" one. This shows that our results are stable against the purity and completeness of the cluster sample, the scale around clusters at which the CW is extracted, and against whether the purity of the filament sample is increased and the statistical size reduced.

In the case of multiplicity (Section 9.1), we also recover a relation with mass. This is somewhat expected (as connectivity and multiplicity are strongly related, Section 6.3), but still interesting to detect, as there is still a degree of variability in the type of critical points to which the maxima matched to clusters are connected to. Also in this case we are able to detect a shallow but present relation between multiplicity and mass which we fit with a "linear" and a "log-log" fit (Section 6.4).

Finally, Figure 2 shows the filament connections-mass relation for the eRASS1 "Pure" sample. In this case the detection is more difficult. In fact we are able to detect a relation only in the case of a persistence threshold of $2\sigma$ and not when a threshold of $3\sigma$ is applied. We conclude that increasing the purity of the filament sample eliminates the signal of a relation between the cluster filament connections and mass. In the $2\sigma$ persistence threshold case, the detection is also possible to a lower redshift than connectivity, i.e. up to $z \leq 0.21$.

## 3 The $[\kappa, \mu, N_{cf}]$-mass relation in context

We thoroughly compare our results to existing studies in the literature. Several works have explored the relation between cluster mass and the number of connected filaments. Although the results of these works are in broad agreement, the methodological differences among them make for a difficult comparison. Among the main differences between the presented works are: the scale on which the filaments are extracted (some works extract the filaments on the full survey area and then match this with the positions of clusters, some others extract the filaments in regions around clusters), the algorithm used and the tuning of algorithm-specific parameters, the measurement of the quantities (some works, e.g., include unmatched clusters in the relation with a connectivity of zero), and the quantity which is related to mass (some works compute the connectivity-mass relation, some others relate multiplicity or filament connections with mass).

We include in this work a summary of the main similarities and differences among the different literature results (Section 8) and we thoroughly compare with our results. We also compare our results obtained with the DESI LS with a measurement of the connectivity-mass, multiplicity-mass, and filament connections-mass relations we achieve in GAMA using spectroscopic redshifts (Section 7). This measurement of the connectivity-mass, multiplicity-mass, and filament connections-mass using spectroscopic redshifts is introduced to have a further reference on the relation when measured using precise galaxy positions to extract the skeleton. It provides a complementary detection to what achieved in the DESI LS with photometric redshifts. However, given the small area of the GAMA survey and the limited number of clusters that fall within its footprint, the uncertainties in our measurements are rather high (Section 7). We

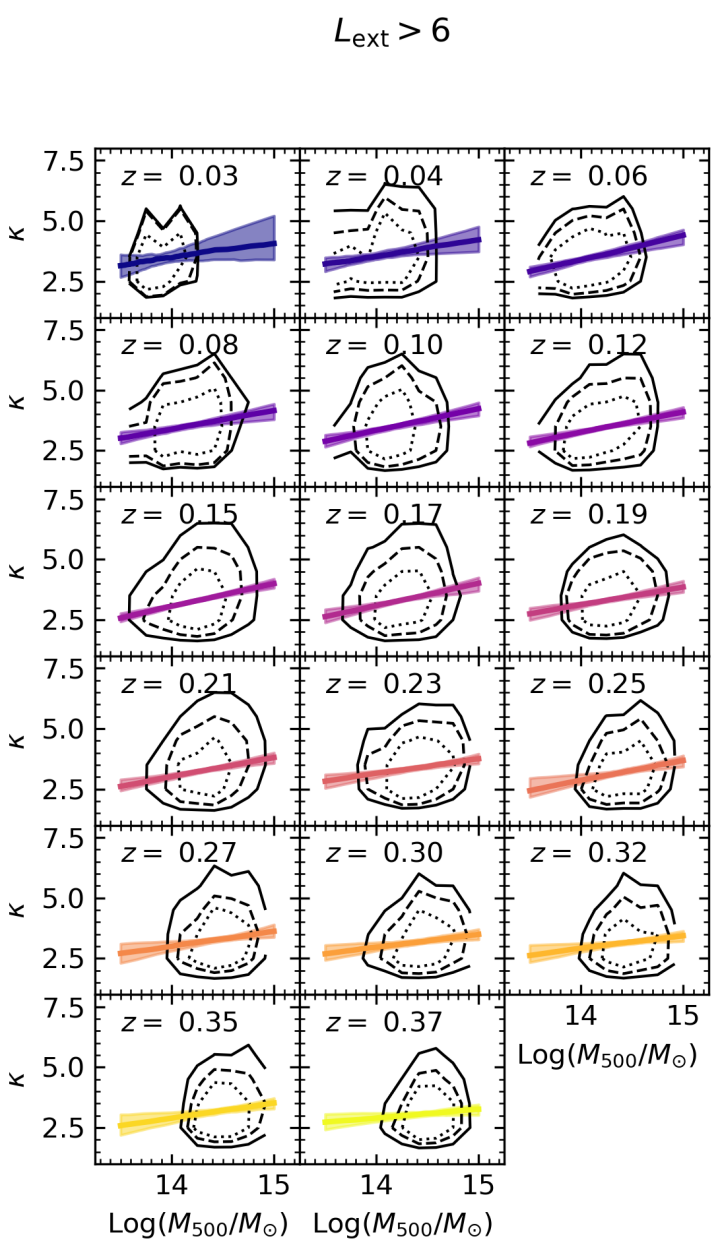


**Fig. 1** The connectivity-mass relation for eRASS1 clusters. In each panel we show a different redshift slice, as marked in the corner. Black contours show the location of the data points (the solid line encircles 90% of the data, the dashed line 75%, and the dotted line 50%). They were derived as the median values of the same contours across the 100 Montecarlo extractions. The line in each panel represents the linear fit to the data, color-coded according to redshift. The line is the median of the individual fits of the 100 Montecarlo extractions. The shaded region shows the range encompassing 68% of the extractions. Only the SD0 case for the Pure cluster sample is shown.

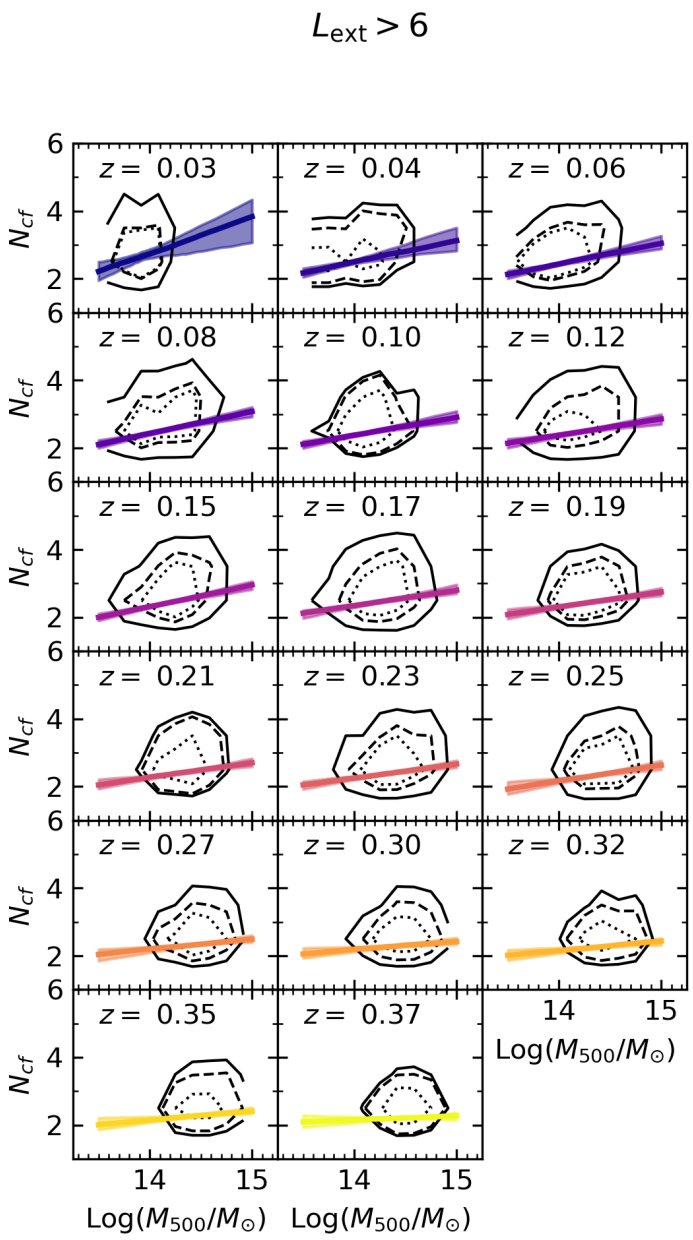


**Fig. 2** Same as Figure 1 but for the filament connections-mass relation.

perform the comparison between the GAMA and DESI LS results with all the combinations we test: the filament extraction using the full survey or the postage stamp approach, the two persistence threshold and smoothing levels, the Large and Pure cluster subsamples, the use of photometric and spectroscopic redshifts for the filament extraction.

Figure 3 shows a comparison of the relations detected in our redshift slices and for the 3D skeleton extraction achieved in GAMA. These figures compare the relations derived in this work with other similar relations obtained from the literature. We sort the works with which we compare our results according to what they measured: connectivity ([18, 34, 41]), multiplicity ([19, 22, 24]) or filament connections in general ([26, 30, 32, 42, 43]). As connectivity and multiplicity are tightly related, we report the curves relative to [19, 22, 24] also in the connectivity-mass relation panels, as we deem a comparison between the two fair enough.

We find that the filament connections-mass relation that we measure in the DESI LS has too shallow a slope to be in agreement with [32, 42, 43]. This is likely due to the very different methods and algorithms (as none of the cited works use DisPerSE) that are employed to measure the filament connections. On the other hand, we are consistent with measurements of the filament connections-mass relation made with similar techniques as us on both the observed and simulated Coma cluster by [26, 30].

In the case of the multiplicity-mass relation, our measurement made on the DESI LS is in excellent agreement with [19, 22, 24], especially in the case of our linear fit. The degree of agreement is still good if we compare the works of [19, 22, 24] to our measurement of the connectivity-mass relation, under the assumption that the multiplicity measured by these works is a good proxy for connectivity (Section 6.3 and, in particular, Figure 10). In the case of connectivity we also find that the measurement we perform for the eRASS1 Pure sample with one level of smoothing of the density field prior to the filament extraction (SD1) for the GAMA skeleton is in agreement with what we derive for the DESI LS. This is in agreement with the findings of Malavasi et al. (under review) where we concluded that the skeleton extracted on the full survey using the DESI LS in the SD0 case was equivalent to the skeleton extracted in GAMA in the SD1 case using spectroscopic redshifts. The connectivity-mass relation we derive in the DESI LS skeleton has a slope in excellent agreement with the work of [18] which however has a normalization very different from all other works in the literature. To be able to better compare trends, we renormalize their relation to pass through the point $(\log(M_{500}/M_{\odot}) = 14.25, \kappa = 3.5)$.

Works such as [34] provide a best-fit value for the connectivity-mass relation which is rather different than what we find in the SD0 case for the DESI LS skeleton, but more in agreement with what we find using GAMA, especially when the eFEDS sample is used. In particular, [34] does not fit a linear relation to the data, but rather a log-log relation. We find that in the case of the DESI LS, a log-log fit (Equation (5)) does not provide a better fit than a linear relation (Equation (4)). In the case of GAMA, however, especially in the case of the eFEDS sample, it returns a function very similar to the one of [34] (this is true also for the Large SD1 sample, not shown here).

We therefore discover the following trend and provide more detail in Section 8. In perfect conditions, when the skeleton of a galaxy or halo distribution is known with

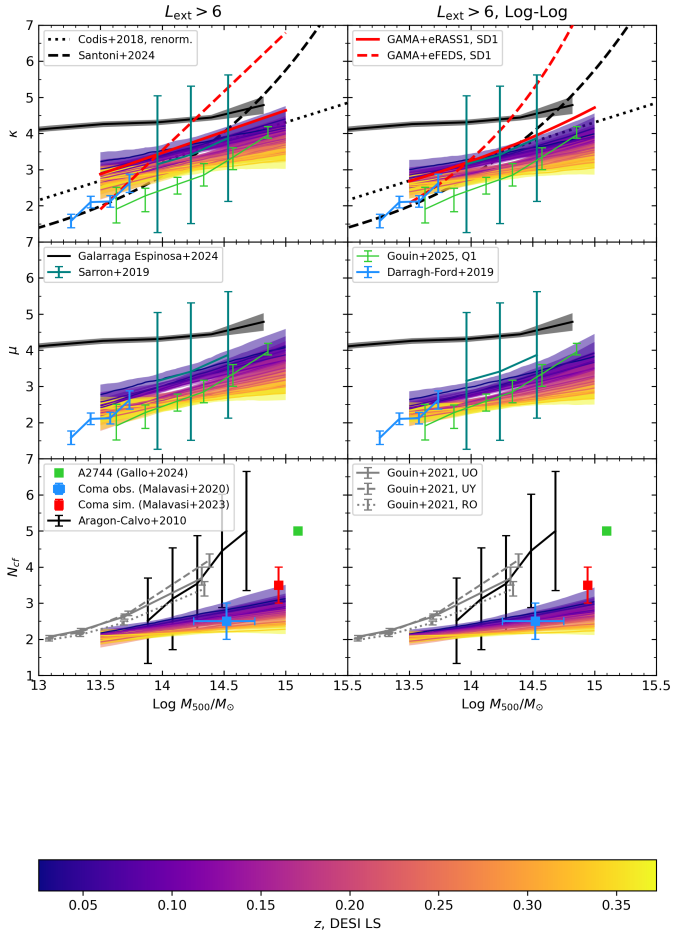


**Fig. 3** Comparison with the literature. Left column: fit performed using Equation (4), right column: Equation (5). Only the eRASS1 Pure sample is shown in the case of the DESI LS skeleton, the eRASS1 Pure and the eFEDS samples are reported in the case of GAMA. Top row: is the connectivity-mass relation, middle row is the multiplicity-mass relation, bottom row is the connections-mass relation. In the bottom panels, the light-blue square refers to the real Coma cluster ([26]), the red square to the simulated Coma cluster ([30]), and the green square to A2744 ([43]). The solid black line is the relation from [42] and its $1\sigma$ uncertainty. The gray lines and associated uncertainties are the filament connections-mass relation measurements of [32] for clusters which are unrelaxed and old (UO, solid line), relaxed and old (RO, dotted line), and unrelaxed and young (UY, dashed line). In the top and middle panels, the solid teal line with uncertainties is the observed multiplicity-mass relation from [19], the solid light blue line is for the groups in COSMOS from [22], while the light green line is the observed multiplicity values from the Euclid Q1 data ([24]). The solid black line and shaded area is the connectivity-mass relation from [41] (at $z = 0$). In the top panels, the dashed black line is the relation derived by [34], while the dotted black line is the theoretical relation of [18], renormalized to pass through the point ($\log(M_{500}/M_\odot) = 14.25$, $\kappa = 3.5$). The solid red line is the connectivity measurement we perform using the GAMA SD1 skeleton and the eRASS1 Pure sample, the dashed red line is the connectivity measured using the GAMA SD1 skeleton and the eFEDS sample. In each panel we report the best fit relation we obtain in each redshift slice, color-coded according to redshift, in the case of the DESI LS skeleton. Associated uncertainties are reported as shaded areas. Masses have been rescaled to $M_{500c}$ for all samples using COLOSSUS.

a high degree of certainty due to the galaxies positions having small errors, the relation between connectivity (or a connectivity proxy such as multiplicity) is described by Equation (5), i.e. it is a relation between the logarithm of connectivity and the logarithm of cluster mass. This is corroborated by results such as [34], which were performed on numerical simulations (The300) and clearly exhibit a log-log behavior. Interestingly, the log-log behavior is not reported by [41], who fail to identify a connectivity-mass relation in this mass range.

When spectroscopic redshifts are used, which allow a skeleton reconstruction with a high degree of certainty, it is still possible to see a log-log relation between connectivity and mass. In our case, we perform such a measurement on GAMA, which exhibits a log-log behavior, but it is plagued by large error bars due to the small cluster sample size. If instead of Equation (5) we use Equation (4), i.e. a linear relation, we get a very steep slope, with a good degree of agreement with the measurement of [34].

Increasing the redshift uncertainty, i.e. lowering the quality of the reconstructed skeleton, e.g. by using photometric redshifts, transforms the relation from log-log to linear (Equation (4)). For example, [22] and [24] use high-precision photometric redshifts and still detect a clear multiplicity-mass relation, but with a linear form rather than a logarithmic one. [19] uses photometric redshifts with a precision comparable to ours in the DESI LS and it is therefore the work we are the most in agreement with. The fact that connectivity is decreased by increased photo-z uncertainty is also confirmed by [22] (see their Section 2.4).

# 4 Discussion and conclusions

Having a statistically robust detection of the connectivity-mass relation is important for several aspects. As is the case with other scaling relations for clusters (e.g., the richness-mass relation), if properly calibrated and cleaned of systematic effects, it could be used in the future as an additional proxy to obtain the cluster total mass. Several works based on simulations ([18, 44–46]) also report that the connectivity-mass relation appears to be sensitive to cosmological parameters, for example those that regulate the equation of state of dark energy, the sum of neutrino masses, or that differentiate between warm dark matter and cold dark matter cosmological models. Moreover, the study of the connectivity-mass relation at different redshifts or for particular classes of sources could lead to the use of this new scaling relation to better understand the process of mass accretion and evolution of clusters, potentially leading to the use of connectivity as a way to connect present-day clusters to their high-redshift progenitors. Finally, it could become a benchmark test for numerical simulations aiming at accurately reproduce the evolution of structures in the Universe.

In order for this relation to become a useful tool in astrophysics it first has to be detected from large cluster samples and to be better understood. For example, it is still not clear what the shape and slope of the relation are, whether it breaks at high cluster masses or at the group regime, whether it presents an evolution with redshift. In order to be able to answer these questions we have to be able to detect the connectivity-mass relation with a sample of clusters numerous enough to be able to divide it in further subsamples, e.g. as a function of redshift. Moreover, while connectivity is the

quantity sensitive to the mix of cosmological parameters as most likely their changes reflect on the topology of the density field, it is also a difficult measurement to achieve in observations, where proxies like multiplicity and filament connections may become more useful.

The novelty in our work lies in the unprecedented scale on which we perform our analysis and the different systematic aspects of the connectivity-mass relation which we explore. Thanks to the large sample size of clusters and a consistent skeleton extraction over a large sky area we are able to not only detect the connectivity-mass relation, but to study it at different redshifts and thoroughly compare it to other results in the literature. We stress that thanks to the use of the eRASS1 sample, we have the same amount of X-ray detected clusters *per redshift slice* that other works use in total. We are, therefore, able to draw the following conclusions:

1. We detect a clear connectivity-mass and multiplicity-mass relation for the eRASS1 clusters using the skeleton detected in the full footprint of the DESI LS with no smoothing of the density field and a $2\sigma$ persistence threshold. Our results are maintained when we raise the persistence threshold to $3\sigma$ or when change the skeleton extraction strategy to just focus on regions around individual clusters.
2. We also detect a filament connections-mass relation, but the slope of this relation becomes too shallow when the persistence threshold is raised, so its detection is less secure.
3. We fit the connectivity-mass and multiplicity-mass relations with a linear fit and derive a slope that appears to become shallower with redshift. We detect the relations up to $z = 0.27$. We attribute the shallower slopes at higher redshift to our reduced ability to extract a reliable skeleton due to the increased photometric redshift uncertainty.
4. We perform a comparison between the connectivity-mass relation detected using spectroscopic redshifts in the GAMA survey and the one detected using photometric redshifts in the DESI LS. We find that the connectivity-mass relation extracted in the GAMA SD1 case is consistent with the DESI LS connectivity-mass relation in the SD0 case. This is supported by the findings of Malavasi et al. (under review).
5. We preform a thorough comparison with the literature and find good agreement between the connectivity-mass and multiplicity-mass relations we derive and several other works. We do not find agreement between our work and the literature when we explore the filament connections-mass relation. This is due to the large variability which is intrinsic in the measurement of this quantity, also based on the various choices of algorithms and techniques to measure filament connections.
6. We identify a trend where the shape of the connectivity-mass relation changes from a log-log relation to a progressively shallower linear relation with increasing uncertainty of the redshift measurements which are used to extract the skeleton of the CW. We plan to investigate this further with the use of controlled experiments such as numerical simulations and mock catalogs.
7. We perform a thorough investigation of our connectivity measurement. We compare 2D and 3D connectivity, finding them in reasonable agreement for the small subsample of clusters that have both quantities measured. We also compare directly connectivity, multiplicity, and filament connections for the same sources, finding

that multiplicity is an excellent proxy for connectivity, but that it is difficult to relate filament connections and connectivity.

This work is but a first step in a new and promising line of research, recently become accessible with the availability of new galaxy surveys and large cluster samples. Future plans for investigations include the use of the new eRASS:5 cluster sample, currently under refinement, and the use of numerical simulation to better analyze systematic effects in the measurement of this relation.

# 5 Methods

## 5.1 Cosmic web extraction

We mainly rely on the CW extraction performed in Malavasi et al. (under review). This is a large-scale (over an area of $19\,342\,\mathrm{deg}^2$) extraction of filaments performed on the DESI LS with the Discrete Persistent Structure Extractor (DisPerSE, [47, 48]). We refer the reader to Malavasi et al. (under review) for a complete description of the detail of the filament extraction process, while we provide here only a brief summary.

The skeleton extraction of Malavasi et al. (under review) uses the DESI LS DR10.1 photometric redshift sample ([39, 40]), complemented with spectroscopic redshifts from the literature ([36]). This is the same galaxy sample that was used to perform the optical identification of the eRASS1 clusters ([35]). They adopt a Montecarlo approach, re-sampling a redshift measurement for each galaxy from a Gaussian distribution centered at that galaxy's estimated photometric redshift and with standard deviation equal to the galaxy's photo-z error. They perform 100 extractions and subsequent filament detections, by dividing the galaxy population of each Montecarlo extraction into four regions of contiguous area, projecting the galaxy population on a plane with a sinusoidal projection, and running DisPerSE in 2D on the projected galaxy population. The galaxy population is divided in 17 redshift slices, designed to be comparable in width to $\pm 1$ times the $1\sigma$ photometric redshift uncertainty and to partially overlap so that the center of one slice becomes the lower boundary of the next. The filament extraction with DisPerSE is performed in 2D for all Montecarlo extractions in each region and redshift slice. Region boundaries in Malavasi et al. (under review) are treated directly by the DisPerSE code, while they extract both a broken down and an unbroken skeleton (i.e. a skeleton which does not contain bifurcations). We make use of both of them here.

In this work, however, we also expand on the skeleton extraction achieved in Malavasi et al. (under review), by exploring new parameter values for the DisPerSE persistence and a different choice of the regions and centers of the redshift slices in which the filaments are extracted. In Malavasi et al. (under review) the persistence threshold of the filament extraction is set to $3\sigma$, while two levels of smoothing of the density field prior to the filament extraction are used (namely 0 smoothing cycles, SD0, and 1 smoothing cycle, SD1). This ensures that only the most reliable filaments are retained at the price of lowering the completeness and statistical size of the filament sample. In this work we have expanded our set of filament extractions to include one where we lower the persistence threshold to $2\sigma$. We report steeper

slopes for the connectivity-mass relation when the $2\sigma$ skeleton is employed, although we recover the same results when the higher-purity $3\sigma$ skeleton is used. We present results obtained with a $2\sigma$ persistence threshold in the main text and those obtained with a $3\sigma$ persistence threshold in Section 9.2.

In addition to this skeleton extraction, we also expand our set of filament samples for the measurement of connectivity by adding one from a complementary perspective. Instead of choosing the slice centers *a priori* and then extracting the skeleton on the entire survey footprint, we extract the CW locally in a region around each cluster. For this, for each cluster, we extract all the galaxies that are in a redshift slice centered at the cluster redshift and with the same thickness as identified in Malavasi et al. (under review), i.e. 170 Mpc (if the cluster redshift is $z_{\rm cl} \leq 0.3$) and 200 Mpc (if $0.3 \leq z_{\rm cl} \leq 0.4$). We also restrict the galaxy selection to only those that are closer to the cluster center than $\max(25{\rm Mpc}, 25 \cdot R_{500})$[1]. In this case too we perform 100 extractions of each galaxy's redshift following the procedure detailed in Malavasi et al. (under review). Therefore for each cluster we have 100 realizations of postage stamp regions, centered on the cluster redshift and location, with galaxies to perform the filament extraction. The filament extraction is done in 2D and the galaxy population is projected using a sinusoidal projection as described in Malavasi et al. (under review). If a cluster has less than 5 galaxies in this postage stamp region we discard it from the rest of the analysis and we do not perform the skeleton extraction around that cluster. We run DisPerSE on each postage stamp region around each cluster, with the same set of parameters used in the case of the entire survey (i.e. persistence thresholds of $2\sigma$ and $3\sigma$ and two smoothing levels, SD0 and SD1). Also in this case we have a broken down and an unbroken skeleton version. We find that the results we obtain with the "postage stamp" skeleton extraction are comparable with those that we obtain with the full survey footprint. In the main text we present only results obtained with the skeleton extraction performed in the full survey footprint ($2\sigma$ persistence threshold). We present the results obtained with the postage stamp skeleton extraction ($2\sigma$ and $3\sigma$ persistence threshold) in Section 9.3.

## 5.2 Cluster selection

The goal of this work is to measure the connectivity-mass relation for a vast sample of X-ray detected clusters, over a large mass and redshift range. To achieve it, we leverage one of the best cluster samples available, i.e. the one extracted from the first year of data taken from the eROSITA All Sky Survey (eRASS1).

The total sample of eRASS1 clusters contains 12 247 objects. Following [35] we select two samples of clusters by performing cuts in the X-ray extent likelihood ($\mathcal{L}_{\rm ext}$) and probability of being contamination ($P_{\rm cont}$). The first sample maximizes sample size at the expense of purity, by selecting all sources with $\mathcal{L}_{\rm ext} \geq 3$ and $P_{\rm cont} \leq 0.8$. This results in 11 522 clusters being selected with a sample purity of 91% (see Table 1 of [35], in the following we refer to this sample also as the "Large" sample). Of these, 9 831 have a measured $M_{500}$ and $R_{500}$. We also select a purer but smaller size sample of 6 752 clusters with $\mathcal{L}_{\rm ext} \geq 6$ to which we apply no cut in $P_{\rm cont}$. [35] cites a purity

[1] We also tested the same approach, but choosing a smaller region of radius $\max(10{\rm Mpc}, 10 \cdot R_{500})$, which yielded comparable results.

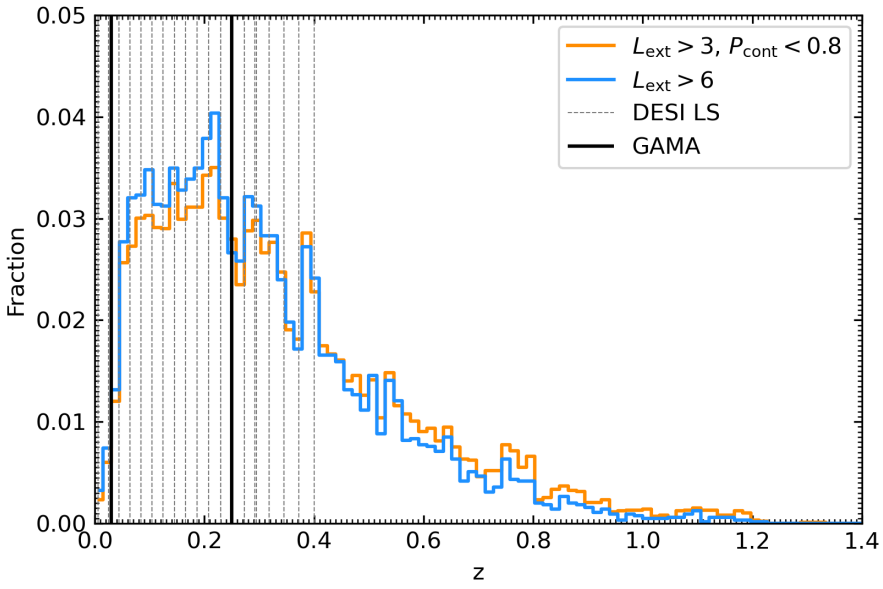


**Fig. 4** Redshift distribution of the cluster sample. The orange line refers to the $\mathcal{L}_{\rm ext} \geq 3$ and $P_{\rm cont} \leq 0.8$ ("Large") sample, while the light blue one to the $\mathcal{L}_{\rm ext} \geq 6$ ("Pure") sample. solid black vertical lines are the redshift limits of the GAMA survey, within which we perform the 3D skeleton extraction. The vertical dashed grey lines are the edges of the overlapping redshift slices in which we divide the DESI LS sample.

of 94% for this sample of clusters, 6 467 of which have a measured $M_{500}$ and $R_{500}$. In the following we refer to this sample also as the "Pure" sample.

Figure 4, shows the redshift distribution for both cluster samples, the one with $\mathcal{L}_{\rm ext} \geq 3$ and $P_{\rm cont} \leq 0.8$ and the one with $\mathcal{L}_{\rm ext} \geq 6$. Both samples show very similar redshift distributions, with a pronounced peak at $z \sim 0.2$ and a long tail reaching up to $z \sim 1.2$. Indeed [35] report a similar median redshift for both samples, of $z = 0.30$ and $z = 0.27$, respectively. In the same image are also the redshift limits for our analysis of the connectivity-mass relation in GAMA (Section 7) and the boundaries of the redshift slices for the main analysis we carry out in the DESI LS (in the case of the skeleton extraction in the full survey footprint, Section 2 and Section 5.1). The CW extracted from the GAMA survey well covers the peak of the cluster redshift distribution. In the case of the DESI LS slices, they manage to sample the cluster redshift distribution up to the beginning of the high-redshift tail, at $z \sim 0.4$. We stress that the limiting factor of our analysis is not the X-ray selected cluster sample, which is able to reach redshifts above 1. On the other hand, we are limited by the availability of suitable surveys with which to perform the CW extraction from the optical galaxy distribution on the scale required to exploit the eRASS1 sample.

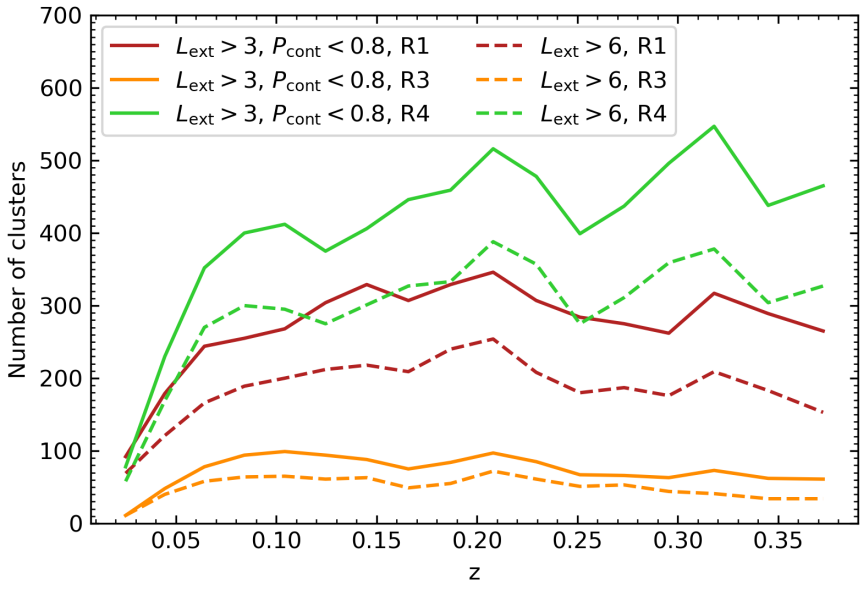


**Fig. 5** Number of clusters in each DESI LS region (see Malavasi et al., under review) as a function of redshift. Solid lines refer to the $\mathcal{L}_{\rm ext} \geq 3$ and $P_{\rm cont} \leq 0.8$ ("Large") sample, while dashed lines to the $\mathcal{L}_{\rm ext} \geq 6$ ("Pure") sample. Red refers to R1, orange to R3, and green to R4. R2 is not covered by the eRASS1 sample.

From the Large and Pure samples we select all clusters that fall inside the redshift range of the GAMA survey (i.e., $0.03 \leq z \leq 0.25$, Section 7) and inside the redshift limits of each of the redshift slices we use for the DESI LS. We also restrict the cluster samples to only those objects that fall within the three GAMA fields (G09, G12, G15) and within each one of the individual regions in which the DESI LS were split to allow the filament extraction (see Figure 2 of Malavasi e al., under review). In particular we highlight that region R2 does not overlap with the German portion of the eROSITA sky, and it is therefore excluded from our analysis.

Figure 5 shows the number of clusters within each redshift slice as a function of redshift. In the case of region R3 the number of clusters is below 100, which is likely due to the smaller size of the region. In the case of regions 1 and 4 the number of clusters is well into the several hundreds per slice up to the highest redshifts we explore. This is a clear improvement with respect to previous studies of connectivity which were limited by the cluster sample size. Indeed, for reference, in this work we have access to the same amount of X-ray selected clusters as the total sample of [19, 22, 24] *per redshift slice* and *in each region* in which the full survey footprint is divided.

Figure 6 shows the mass distribution for the various cluster samples and sub-samples. Mass distributions for both the total samples ($\mathcal{L}_{\rm ext} \geq 3$, $P_{\rm cont} \leq 0.8$ and $\mathcal{L}_{\rm ext} \geq 6$) are very similar and span the unique mass range of $5 \times 10^{12} \div 2 \times 10^{15} M_{\odot}$.

There is a slight tendency for the Large sample to be distributed at smaller masses. We also show the mass distribution for the clusters located in the three GAMA fields combined and within the GAMA redshift range. Although the number of clusters is very low, they are distributed in the same mass range and cover all mass values, up to masses of $M_{500} \sim 5 \times 10^{14} M_{\odot}$. Finally, we present the mass distributions for clusters within regions R1, R3, and R4 of the DESI LS (combined together) and for each redshift slice. Again the mass distribution of clusters in each redshift slice covers roughly the entire mass range. It can also be seen how the peak of the distributions gradually shifts to higher cluster masses with increasing redshifts. This is a selection effect, as only the most massive and luminous clusters will likely be detected at higher redshift. In general, we do not find any major systematic effect in the mass distribution of the clusters we consider for our analysis. In order to perform an analysis of connectivity, multiplicity, and filament connections we select only clusters with masses in the range $13.5 \leq \log(M_{500}/M_{\odot}) \leq 15$. We therefore restrict ourselves to this mass range for what concerns the following sections and the results presented in Section 2.

# 6 Matching the eROSITA clusters to the DisPerSE critical points and measuring connectivity

The study of the topology of the galaxy density field is useful to understand how structure formation proceeds in the Universe (e.g., [49]). Under the assumption that clusters of galaxies are located at the nodes of the CW, that they are associated with maxima of the galaxy density field, and that cluster mass and node (over)density are strongly correlated, a connectivity-mass relation is expected to emerge for samples of galaxy clusters. The measurement of this connectivity-mass relation for the eROSITA clusters is achieved via three subsequent steps, which are explained in detail in the remainder of this section. We summarize them here.

1. **Matching eROSITA clusters with DisPerSE critical points.** The DisPerSE output consists in a map of maxima of the density field together with their connected filaments. This map includes, of course, other critical points (saddles, minima, and bifurcations). In order to be able to measure the number of filaments connected to a given eROSITA cluster, the first step is therefore to match the sample of X-ray detected clusters to the maxima as output by DisPerSE.
2. **Measuring connectivity, multiplicity, and connections.** After each eROSITA cluster has been matched to a maximum of the density field, the filaments connected to that maximum can be counted to measure the cluster connectivity, multiplicity, or connections. These are three distinct concepts that will be introduced in the relevant section.
3. **Characterizing the connectivity-mass relation.** The last step consists in deriving the connectivity-mass (or multiplicity-mass, or connections-mass) relation, analyzing its slope, and comparing with existing measurements in the literature.

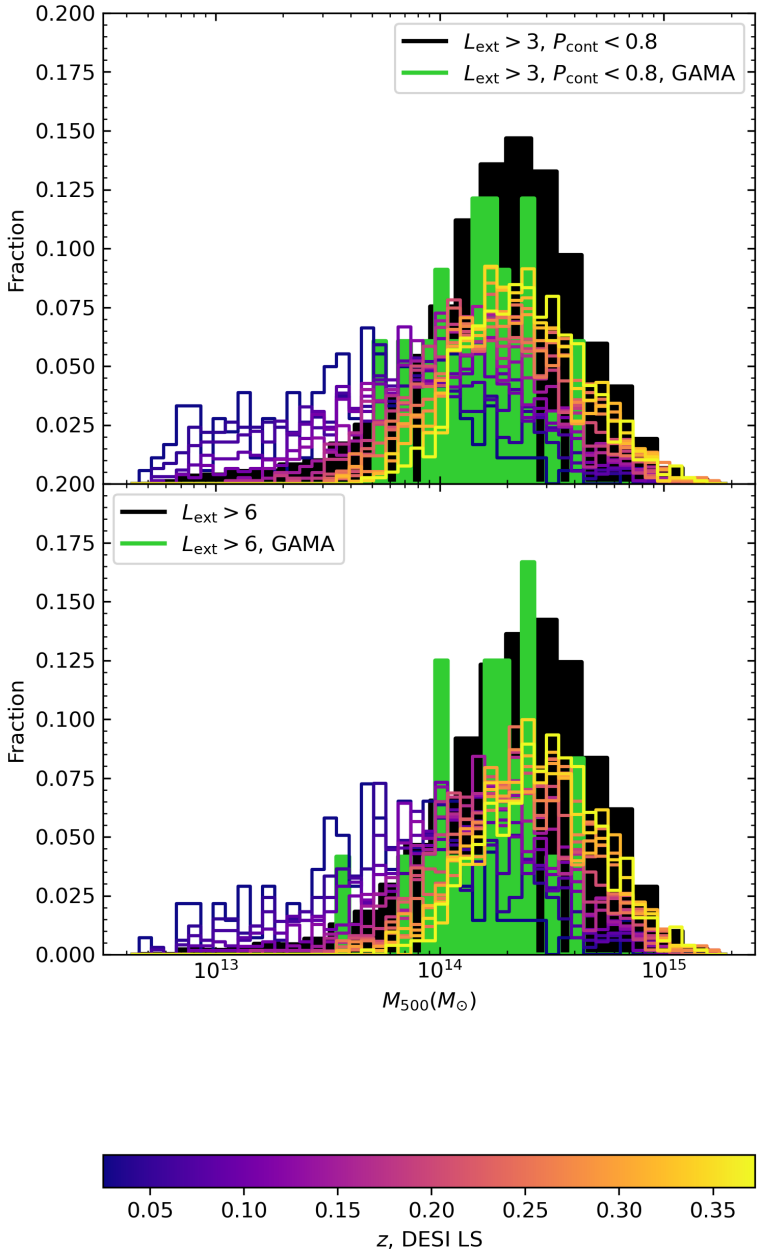


**Fig. 6** Mass distribution of the clusters in the various samples. The top panel refers to the $\mathcal{L}_{ext} \geq 3$ and $P_{cont} \leq 0.8$ ("Large") sample, while the bottom panel to the $\mathcal{L}_{ext} \geq 6$ ("Pure") sample. In each panel, the black histogram is the starting sample, the green histogram are clusters within the GAMA fields and redshift limits, while the colored lines are the clusters in the DESI LS area (all regions combined), and within the limits of each redshift slice, color-coded according to the center of the redshift slice to which they belong.

In broad terms, we expect clusters to be located at the nodes of the CW. Galaxy clusters, especially massive ones with confirmed presence of hot X-ray-emitting Intracluster Medium (ICM) are overdense peaks of the density field, which should be univocally identified as maxima in a density field analysis.

The DisPerSE algorithm provides such an analysis of the density field and outputs catalogs of filaments starting from the critical points they are connected to. In the following, we mainly focus on the two types of critical points which we deem the most relevant for galaxy clusters: maxima and bifurcations. We choose these critical points because we expect galaxy clusters to be associated with a maximum of the density field or a node where filaments intersect. We present in this section the results obtained with the skeleton extracted in the full survey volume with a $2\sigma$ persistence. We present the results obtained with a $3\sigma$ persistence threshold in Section 9.2 and the results obtained with the postage stamp skeleton extraction in 9.3.

The first step in the matching of eRASS1 clusters to critical points in the DisPerSE analysis of the density field is a proper treatment of the skeleton to extract critical points suitable for the matching. We start by using the unbroken skeleton and identify all critical points which are given an index different from that of a maximum, saddle, or minimum. These residual critical points are boundary critical points left over by the boundary cleaning operated by DisPerSE. We spatially match the identified boundary points of the unbroken skeleton with their corresponding ones in the broken down skeleton and mark them so that they cannot be matched to a cluster. We note, however, that we do not remove them so as not to change the topology of the skeleton and the interconnected information output by DisPerSE. As such, it is still possibile that a filament connected to a critical point matched to a cluster has at the other hand a critical point marked as boundary. We then de-project the positions of the critical points to bring them back in Equatorial coordinates. This is done by inverting Equation 1 of Malavasi et al. (under review). Starting from projected coordinates $x$ and $y$, we derive:

$$\mathrm{Dec} = y \tag{1}$$

$$\mathrm{RA} = \frac{x}{\cos(y)} + \mathrm{RA}_0 \tag{2}$$

where $\mathrm{RA}_0$ is the reference central meridian, for which we take the same value used in Malavasi et al. (under review).

We focus on two types of match between eRASS1 clusters and critical points: in one case we try to associate only maxima to clusters, in a second case we try to associate all critical points without distinction. We therefore extract a subsample of critical points composed of only maxima for both the broken down and the unbroken skeleton, while by construction the maxima, bifurcation, and saddle mixed sample can only be matched to clusters using a broken down skeleton.

## 6.1 Matching maxima

For each cluster, we identify the maximum in the unbroken skeleton maxima subsample that has the smallest distance from the cluster center, in equatorial coordinates. We

consider this maximum to be the one associated with the considered cluster. We match this maximum to a corresponding one in the broken down skeleton, by looking for exact matches in terms of spatial coordinates. This matching is required to make sure that the maxima in the broken down and unbroken skeleton perfectly correspond as expected. We repeat the matching between a cluster and the maxima of the density field for all clusters within each redshift slice and all Montecarlo extraction. Thus for each sample of clusters located within each redshift slice we obtain 100 matched maxima, one per Montecarlo extraction.

Having established which maximum is matched to each considered cluster and how far from the cluster center the chosen maximum is, we establish if the distance between the maximum position and the cluster center is larger than a factor $n$ times the cluster $R_{500}$ (with $R_{500}$ measured in deg on the plane of the sky, not in the projected coordinate frame so as not to distort cluster shapes). Figure 7 shows the fraction of clusters that have their associated maximum closer to the center than $n \times R_{500}$ as a function of $n$ for the various cluster samples ($\mathcal{L}_{\rm ext} \geq 3$, $P_{\rm cont} \leq 0.8$ and $\mathcal{L}_{\rm ext} \geq 6$) and for the two smoothing levels of the skeleton (SD0 and SD1) for all redshift slices. Each line in this plot is the median of the 100 Montecarlo extractions.

This figure clearly shows how the process of associating a maximum of the density field to each cluster is not straightforward. First of all, in the SD1 case, the fraction of clusters having their closest (associated) maximum within $10 \times R_{500}$ (a considerable distance) is lower at all redshifts than in the SD0 case, with 70% of clusters or less having their associated maximum within $5 \times R_{500}$. The situation is even worse if the consider the $3\sigma$ skeleton (extracted on the full survey volume, Figure 17). Considering the analysis made in Malavasi et al. (under review) together with the fact that the fraction of clusters having their matched maximum within $10 \times R_{500}$ is below 40% at all redshifts in the $3\sigma$ skeleton, we discard results obtained with the SD1 skeleton in the full survey footprint from this work.

In the case of SD0, all fractions increase continuously with the factor $n$, as expected. At all redshifts, more than half of the clusters have their closest associated maximum within at most $R_{500}$. At intermediate redshifts, the fraction becomes close to 100% for $n \geq 5$.

## 6.2 Matching all critical points

In the case of the maxima, bifurcations, and saddles subsample we proceed in a slightly different way, mainly to be consistent with previous works ([26, 30]). In particular, instead of looking for the closest critical point to each cluster's center, we identify all critical points that are located within $n \times R_{500}$. In this case we do not consider the cluster to be matched with the closest critical point to that cluster center, but to be associated with all critical points, regardless of their type, which are located within $n \times R_{500}$.

Figure 8 shows the fraction of clusters that have no critical points of any kind (including saddles and minima) within $n \times R_{500}$. As it was the case with Figure 7, these fractions continuously drop with increasing value of the factor $n$. In the SD1 case more than 20% of clusters have no critical point whatsoever within $5 \times R_{500}$. In the $3\sigma$ persistence case, more than 40% of clusters have no critical point within

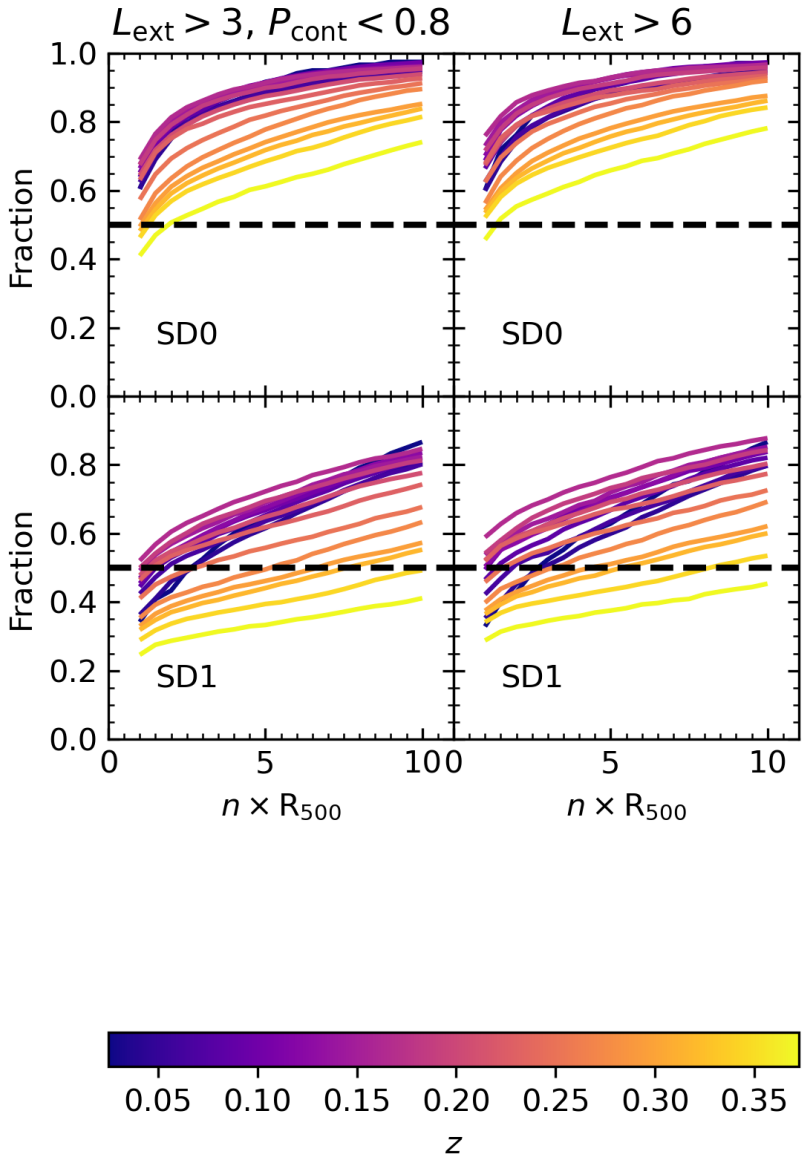


**Fig. 7** Fraction of clusters with at least one associated maximum within $n \times R_{500}$ as a function of $n$. The two columns refer to the different cluster samples (Large, left column and Pure, right column, respectively), while the two rows refer to the different smoothing levels (SD0, top row, and SD1, bottom row, respectively). Lines refer to the various redshift slices in which we perform our analysis and are color-coded according to the redshift of the slice center. The black dashed line highlights a fraction of 50% for reference. The skeleton was extracted in the full survey volume with a persistence of $2\sigma$.

$10 \times R_{500}$, which again points us in the direction of disfavoring this smoothing level. In the SD0 case, for low and intermediate redshift slices the fraction of clusters that have no critical point within $R_{500}$ is significantly below 50%.

## 6.3 Measuring Connectivity, Multiplicity, and Filament connections for the eROSITA clusters

After having performed a successful match between the DisPerSE output in terms of critical points and the eROSITA clusters, we proceed to measure connectivity, multiplicity, and filament connections for the X-ray clusters. Although the terms have often been conflated in the literature, they actually refer to different topics.

Following [18], connectivity ($\kappa$) is defined as the number of filaments that depart from a maximum and that reach saddle points in an unbroken skeleton (i.e. a skeleton where bifurcation points are not present). In this framework, if two filaments depart from the same maximum and reach different saddles, but spatially overlap for part of their path, they will be counted as distinct.

The measurement of connectivity is well suited to be carried out in numerical simulations, where a complete view of the skeleton is available and systematic effects are under more control. However, it is difficult to reconcile the measurement of connectivity with what can be done in observations. For this reason, the measurement of multiplicity ($\mu$) was introduced (see Equation 8 of [18]). This is defined as the number of filaments connected to a maximum that reach different saddles in an unbroken skeleton minus the number of same filaments that reach bifurcations in a broken down version of the same skeleton. Multiplicity and connectivity are related by:

$$\mu = \kappa - n_{\rm bif} \tag{3}$$

where $n_{\rm bif}$ is the number of filaments that reach a bifurcation from a given maximum instead of a saddle in a broken down version of the skeleton.

In an astrophysical context, however, performing the distinction between multiplicity and connectivity is not always possible. This is true, for example, if the number of filaments connected to a cluster is obtained by visual identification, or by using a CW detection algorithm which is unable to identify maxima and saddles (e.g. because the method used is different from a Hessian or topological analysis of the density field, such as e.g. graph theory and percolation). Several works have thus resorted to count all filaments connected to a structure (e.g. a cluster) by associating that structure to (sometimes multiple) critical points without distinguishing their type and then counting all the filaments connected to the critical points associated to the structure without distinguishing the critical point at the other end (i.e. without checking whether it is a saddle or a bifurcation). We call this (astrophysically motivated) hybrid measurement of connectivity/multiplicity "counting the filament connections" of a cluster, to keep it distinct from the measurement of proper multiplicity and connectivity, for clarity. In this work we measure both connectivity, multiplicity, and filament connections for the eROSITA clusters. In the main text (Section 2), we present only the result for connectivity and filament connections, while we present the measurements of multiplicity in Sections 9.2 and 9.3. Here, we also compare the measurement of connectivity,

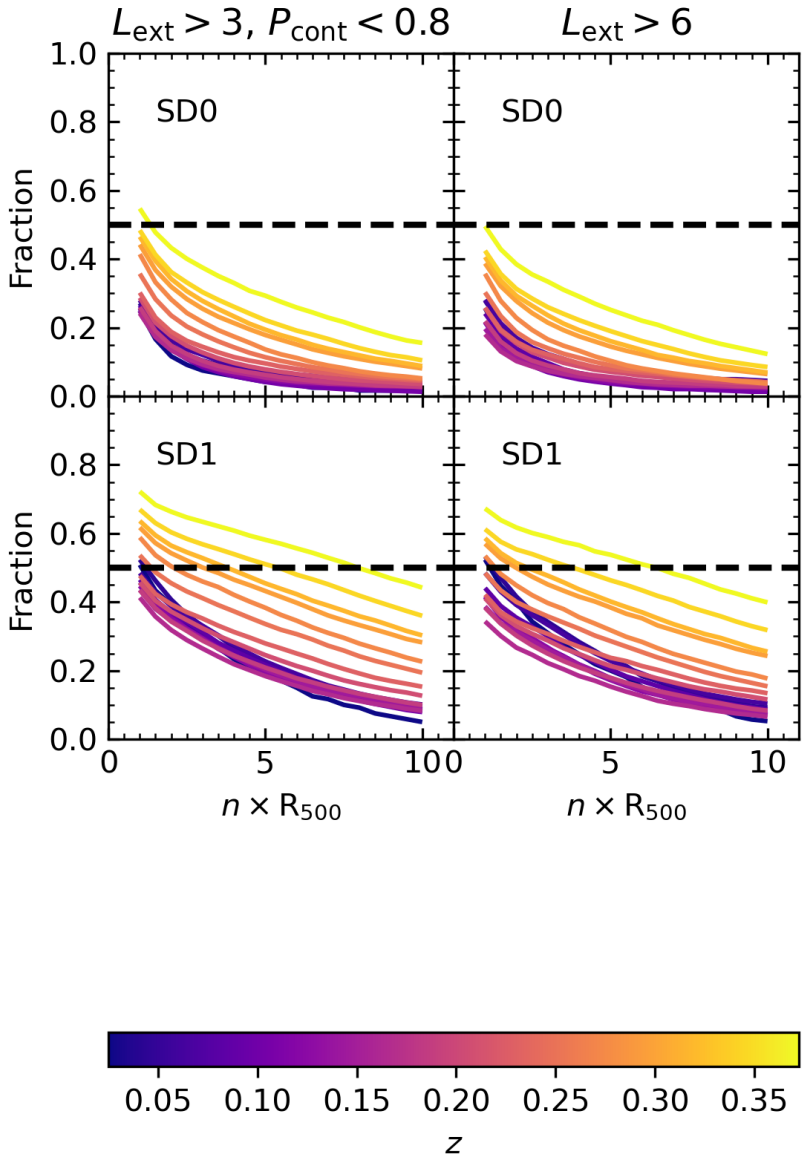


**Fig. 8** Fraction of clusters with no associated critical point within $n \times R_{500}$ as a function of $n$. The two columns refer to the different cluster samples (Large, left column and Pure, right column, respectively), while the two rows refer to the different smoothing levels (SD0, top row, and SD1, bottom row, respectively). Lines refer to the various redshift slices in which we perform our analysis and are color-coded according to the redshift of the slice center. The black dashed line highlights a fraction of 50% for reference. The skeleton was extracted in the full survey volume with a persistence of $2\sigma$.

multiplicity, and filament connections to understand whether they actually trace the same cluster property or not.

In this work we do not measure the absolute connectivity of each cluster, but rather we measure the connectivity at a distance from the cluster center. This approach ensures that only large-scale filaments that actually branch out of the cluster are counted and not smaller filaments that may be due to the particular shape of the density field in a high-density region.

For each redshift slice in the case of the DESI LS skeleton, we choose the smallest factor $n_\kappa$ for which at least 50% of clusters have their associated maximum within $n_\kappa \times R_{500}$ (see Figure 7). We note that for the case of the skeleton extracted in the full survey footprint with a persistence threshold of $2\sigma$ we have $n_\kappa = 1$ for all clusters. However, this is not the case when a higher persistence threshold is used (Section 9.2 or the postage stamp skeleton is used 9.3). In case a factor cannot be identified, we use $n_\kappa = 10$, i.e. the maximum value we consider in our analysis. Results in the main text are presented for the case $n_\kappa = 1$, i.e. with a connectivity measured at $R_{500}$. We then measure a cluster's connectivity as the number of filaments in the unbroken skeleton connected to the associated maximum for which the distance from the associated maximum to the saddle (and saddle only) at the other end of each filament is larger than $n_\kappa$ times the associated cluster's $R_{500}$.

Having achieved a measurement of connectivity, we switch to the measurement of multiplicity. For each maximum associated to each cluster we identify all filaments that instead of reaching a saddle reach a bifurcation in the broken down version of the skeleton, where the bifurcation is also located at a distance from the maximum larger than $n_\kappa \times R_{500}$ with the factor $n_\kappa$ identified as described above and the $R_{500}$ of the associated cluster. We then use Equation 3 to measure multiplicity for the eRASS1 clusters.

Finally we measure the filament connections to each cluster. In this case we do not consider only the maximum associated to each cluster, but rather consider all critical points associated to each cluster as mentioned above. For each redshift slice, we select a factor $n_{\rm fc}$ as the smallest possible value of $n$ for which the fraction of clusters that have no critical point of any kind associated to them is at most 50% (see Figure 8). As in the case of connectivity, in the case of the skeleton extracted in the full survey footprint with a $2\sigma$ persistence we have $n_{\rm fc} = 1$, but this is not the case for other persistence thresholds and in the postage stamp case. We then measure filament connections for each cluster. For each critical point associated to a given cluster we count the number of filaments connected to that critical point (regardless of whether it is a maximum, bifurcation, or saddle[2]) which are connected to another critical point of any type (again maxima, bifurcations, or saddles) located further away from the associated critical point than $n_{\rm fc}$ times the cluster $R_{500}$. In this way, for each cluster we have a set of associated critical points, each with a measured number of connected filaments. The final number of filament connections for the cluster is the sum of the filament connections for the associated critical points. We use for this measurement only the unbroken skeleton.

[2]Minima and type-1 saddles, by construction, can be associated to a cluster but have no filaments connected to them.

Figure 9 shows the $\kappa$, $\mu$, and the number of filament connections distributions for the eRASS1 clusters. This figure was constructed selecting only a subset of clusters for each redshift slice. By construction, each cluster falls at most inside two overlapping redshift slices, but the cluster redshift will be closer to the redshift of the center of only one of the two redshift slices. For each redshift slice, we therefore report here only the clusters that have their redshift closest to the slice center redshift.

Filament connections is the quantity that is distributed at smaller values, peaking at $\sim 2$, while connectivity and multiplicity are distributed in a more spread-out way, reaching values of more than $\kappa \sim 5$ and $\mu \sim 5$. In general, we find that filament connections have a smaller dynamic range in the values that they can take per cluster, while connectivity and multiplicity vary more widely. In the case of the DESI LS there appears to be a mild evolution with redshift of the normalization of the distributions, although their shape is generally preserved.

We note that a few clusters have a connectivity of 1. We consider these cases to be topological defects of our skeleton (see e.g. the discussion in [50]). Clusters can be associated to a maximum that is connected to only one filament, in which case they are removed from our analysis of the connectivity, multiplicity, and filament connections, as are clusters which are not matched to a critical point.

We then check how much connectivity, multiplicity, and filament connections are related one to another. The idea is to understand whether filament connections and multiplicity can be considered as proxies of true connectivity or whether they have to be treated differently. Indeed connectivity and multiplicity are related by Equation (3). We therefore expect a strong correlation between the two. We check how much these quantities are linked to the cluster filament connections. As filament connections are somewhat easier to compute than connectivity and multiplicity, we aim at understanding how good of a proxy they are for true cluster connectivity.

Figure 10 shows the comparison between connectivity, multiplicity, and filament connections for the eRASS1 clusters. As expected there is a strong relationship between connectivity and multiplicity, with the latter being always smaller than the former, but both along the 1:1 line. On the other hand, the filament connections show a large scatter with respect to both connectivity and multiplicity, with no detectable relationship. We argue that, although the measurement of filament connections to clusters in an astrophysical sense is an important measurement, it can seldom be used as a proxy for proper connectivity without a more in-depth analysis. We highlight that this could be at the origin of the difference between the measurement performed for Coma in [26] and other works in the literature.

### 6.4 Fitting the $[\kappa, \mu, N_{cf}]$-mass relation

We fit the connectivity-mass, multiplicity-mass, and filament connections-mass point distributions with the linear relation

$$[\kappa, \mu, N_{cf}] = m_{[\kappa,\mu,\mathrm{fil}]} \log(M_{500}/M_{\odot}) + q_{[\kappa,\mu,\mathrm{fil}]} \tag{4}$$

where the notation $[\kappa, \mu, N_{cf}]$ means that we perform the fit separately for $\kappa$, $\mu$, and $N_{cf}$.

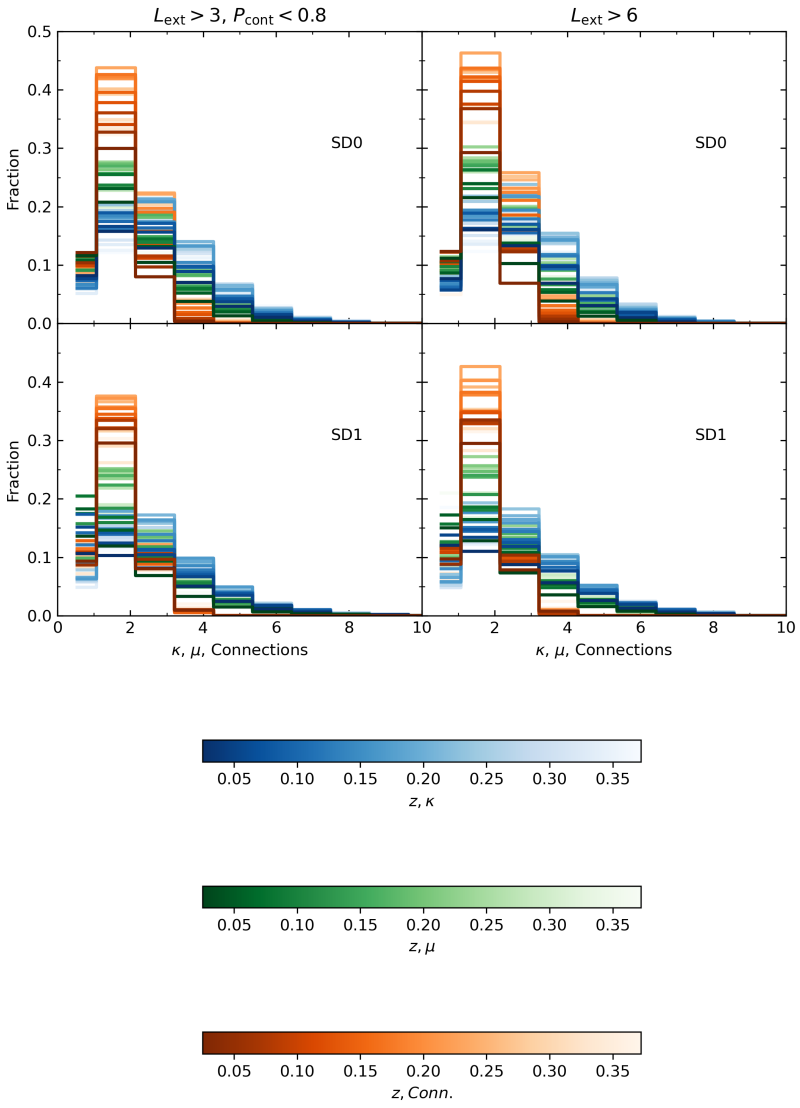


**Fig. 9** $\kappa$, $\mu$, and the number of filament connections distributions for the eRASS1 clusters in the case of the DESI LS skeleton when the extraction is done on the full survey. Left column is the Large sample, right column is the Pure sample. Top row is the SD0 case, bottom row is the SD1 case. In each panel blue shades refer to cluster connectivity, green shades to multiplicity, and orange shades to filament connections. Progressively lighter lines refer to higher redshifts.

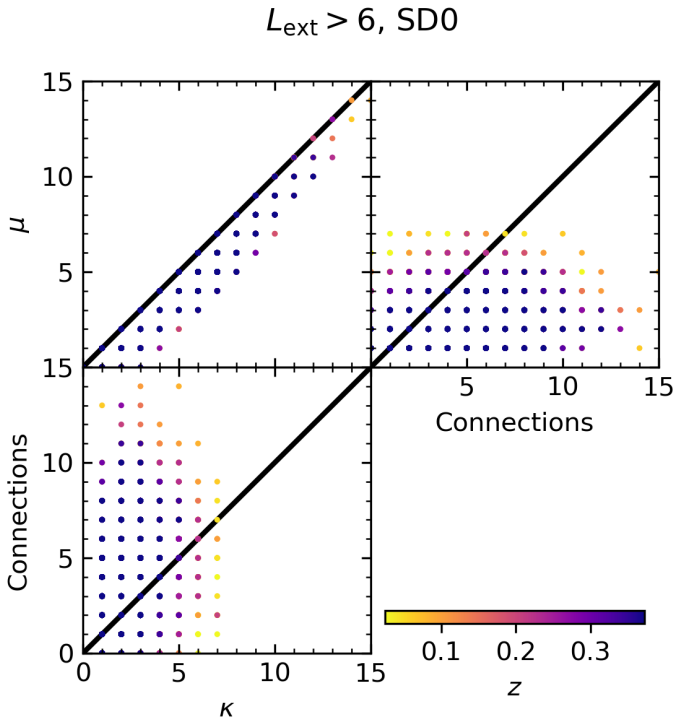


**Fig. 10** Comparison of connectivity, multiplicity, and filament connections for the Pure eRASS1 cluster sample, with the skeleton extracted in 2D in the DESI LS survey. Top panel refers to the case where the skeleton is extracted in the full survey, bottom panel to the postage stamp skeleton case. Only the SD0 case is shown. In each panel we present the cluster distribution in the $\kappa$-$\mu$ plane (top left corner), the connections-$\mu$ plane (top right corner), and the connections-$\kappa$ plane (bottom left corner). The black diagonal line shows the 1:1 line for reference, points are individual eRASS1 clusters (median of 100 extractions). Points are color-coded according to the redshift of the center of the redshift slice to which they belong. We note that, as connectivity, multiplicity, and connections can only take discrete values, several cluster points lie on top of each other. In this case only the highest redshift slices are shown.

To better compare this work with existing literature and to test all scenarios, we also fit our measurements with Equation (5).

$$\log([\kappa, \mu, N_{cf}]) = m^{\log}_{[\kappa,\mu,\mathrm{fil}]} \log(M_{500}/M_{\odot}) + q^{\log}_{[\kappa,\mu,\mathrm{fil}]} \tag{5}$$

In Section 2 we present only the case of Equation (4) in Figures 1 and 2. Equation (5) becomes relevant for the comparison with literature, shown in Figure 3.

We quantify the presence of a connectivity-mass and of a multiplicity-mass relation by analyzing the trend of the fit parameters $m_{[\kappa,\mu,\mathrm{fil}]}$ and $q_{[\kappa,\mu,\mathrm{fil}]}$ for connectivity, multiplicity, and filament connections as a function of redshift. We report these values in Figure 11

Figure 11 shows the values of $m_{[\kappa,\mu,\mathrm{fil}]}$ and $q_{[\kappa,\mu,\mathrm{fil}]}$ for the DESI LS full-footprint skeleton in the SD0 case with a $2\sigma$ persistence threshold as a function of redshift.

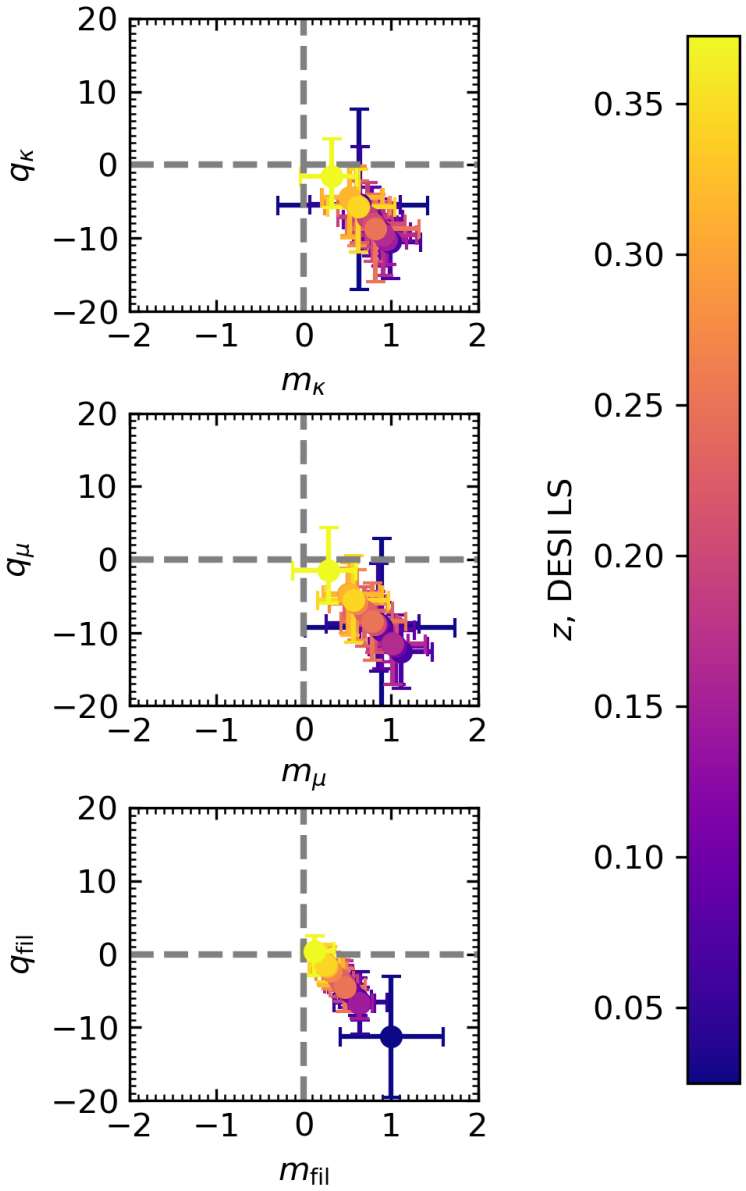


**Fig. 11** Best fit parameters. Top panel: $m_\kappa$ vs. $q_\kappa$, middle panels: $m_\mu$ vs. $q_\mu$, bottom panel: $m_{\rm fil}$ vs. $q_{\rm fil}$. In each panel points are color-coded according to redshift. Error bars show the range covering 68% of the parameter values across Montecarlo extractions, with each point showing the median value of the parameters. Grey lines show a value of 0 for the parameters for reference.

There is a clear positive correlation between mass and the various quantities explored, with a positive $m_{[\kappa,\mu,\mathrm{fil}]}$ and a negative $q_{[\kappa,\mu,\mathrm{fil}]}$. The slope of the relation becomes shallower with redshift. We have visually compared the linear case with the log-log case and found no significant difference (see Figure 3).

# 7 Measuring the $[\kappa, \mu, N_{cf}]$-mass relation in GAMA

We perform the same connectivity, multiplicity, and filament connections analysis using the GAMA survey. As in this case the skeleton was extracted using spectroscopic redshifts, we use this as a reference for further validating our results. We summarize in this section the setup of this test.

## 7.1 Skeleton extraction in GAMA

Malavasi et al. (under review) also performed an extraction of the filaments of the CW with DisPerSE using the spectroscopic sample of the Galaxy Evolution and Mass Assembly survey DR4 (GAMA [51, 52]). While in Malavasi et al. (under review) this skeleton was used to validate the skeleton extraction performed in the DESI LS, in the present work we use it to validate the measurement of the connectivity-mass relation. In the case of GAMA the filament extraction is performed in 3D in the survey volume, in the three GAMA fields G09, G12, G15 separately (combined area of $180\,\mathrm{deg}^2$). An algorithm ([53, 54]) for the compression of the Finger of God redshift distortion is applied to detect distorted groups and compress them along the line of sight so that they are not mistaken for filaments. The persistence threshold is set to $3\sigma$. Considering that the use of spectroscopic redshifts allows for a secure extraction of filaments in what is a very well explored field, we do not test lower persistence thresholds like we do in the DESI LS case. On the other hand, we test two smoothing levels (SD0 and SD1). Boundary treatment is done as in the DESI LS case. The skeleton in GAMA too is extracted in a broken down and unbroken version, both of which are employed here.

## 7.2 Cluster selection

Table 1 presents the number of clusters belonging to the Pure and Large samples (as defined in Section 5.2) that are located in the three GAMA fields. The number of clusters within the GAMA footprint is very small, always below 20 (and in the G09 case below 5), which limits the reach of our analysis using this spectroscopic survey.

Given that the small number of sources in the eRASS1 sample within the survey area is a limiting factor in the significance of the measurement of the connectivity-mass relation that we aim to obtain, we resorted to test with a deeper set of data whether we could recover the same results that we obtain with the shallower eRASS1. The eROSITA Final Equatorial-Depth Survey (eFEDS, [55, 56]) is a survey of $\sim 140\,\mathrm{deg}^2$ achieved during the Performance Verification phase of eROSITA. It reaches the same sensitivity expected for the end-of-survey observations of eRASS:8 and it overlaps in full with the G09 field of the GAMA survey.

From the initial sample of 542 eFEDS clusters with $\mathcal{L}_{\mathrm{ext}} \geq 5$ and $\mathcal{L}_{\mathrm{det}} \geq 6$ presented in [55] we select the 59 that are found within the GAMA redshift range and GAMA

**Table 1** Number of clusters belonging to the $\mathcal{L}_{\rm ext} \geq 3$ and $P_{\rm cont} \leq 0.8$ ("Large") and to the $\mathcal{L}_{\rm ext} \geq 6$ ("Pure") sample in each of the GAMA fields.

| Field | $\mathcal{L}_{\rm ext} \geq 3$, $P_{\rm cont} \leq 0.8$ | $\mathcal{L}_{\rm ext} \geq 6$ |
|---|---|---|
| G09 | 3 | 4 |
| G12 | 12 | 7 |
| G15 | 18 | 13 |

field G09 area. We do not impose any further cut in $\mathcal{L}_{\rm ext}$ or $\mathcal{L}_{\rm det}$ to maximize sample size. Table 2 of [55] quotes a purity of 80% and a completeness of 40% for this sample.

### 7.3 Measuring Connectivity, Multiplicity, and Filament connections with the GAMA skeleton

We proceed in the same way as in the case of the DESI LS, with the exception that clusters $R_{500}$ are not considered as measured in deg on the plane of the sky, but in Mpc in 3D. Figure 12 shows the fraction of clusters that have their closest associated maximum within $n \times R_{500}$ as a function of $n$. In this case we consider three cluster samples, the eRASS1 samples considered also in the case of the DESI LS skeleton ($\mathcal{L}_{\rm ext} \geq 3$, $P_{\rm cont} \leq 0.8$ and $\mathcal{L}_{\rm ext} \geq 6$) and the eFEDS sample (lines corresponding to the eFEDS sample are reported in all panels for reference, but they do not vary across columns). With GAMA we find results consistent with what found in the DESI LS case, where a fraction of 50% or more clusters in the eRASS1 case has the closest associated maximum at a distance of $3R_{500}$ or more. In the case of eFEDS, the fractions are lower with the 50% fraction line being crossed at a value of $5R_{500}$.

Figure 13 shows the fraction of clusters in the GAMA fields that have no critical points of any kind located within $n \times R_{500}$. Similarly to the case of the DESI LS, the fractions for the GAMA survey quickly drop to zero, especially in the case of eRASS1. At $2R_{500}$ already less than 50% of the clusters have no matched critical points. Fractions remain slightly higher for the eFEDS sample than the eRASS1 ones.

We measure connectivity, multiplicity, and filament connections for GAMA in the same way as we did for the DESI LS skeleton, i.e. at a distance from the cluster center, set by the cluster $R_{500}$ multiplied by a factor $n_\kappa$ or $n_{\rm fc}$ identified as those for which the fraction of clusters having at least one associated maximum (or no critical points associated) is greater (lower) than 50%. Figure 14 shows the connectivity-mass, multiplicity-mass, and filament connections-mass relation for the eRASS1 and eFEDS clusters using the GAMA skeleton. We recover a connectivity-mass relation and a multiplicity-mass relation for all cluster samples in the SD0 case. In the SD1 case, we are able to recover only the connectivity-mass relation and multiplicity mass relation for the eFEDS clusters and for the Large eRASS1 sample (this latter, however, with a shallower slope and larger error bars). We never recover a connections-mass relation for GAMA as the error bars on the fit parameters are too large.

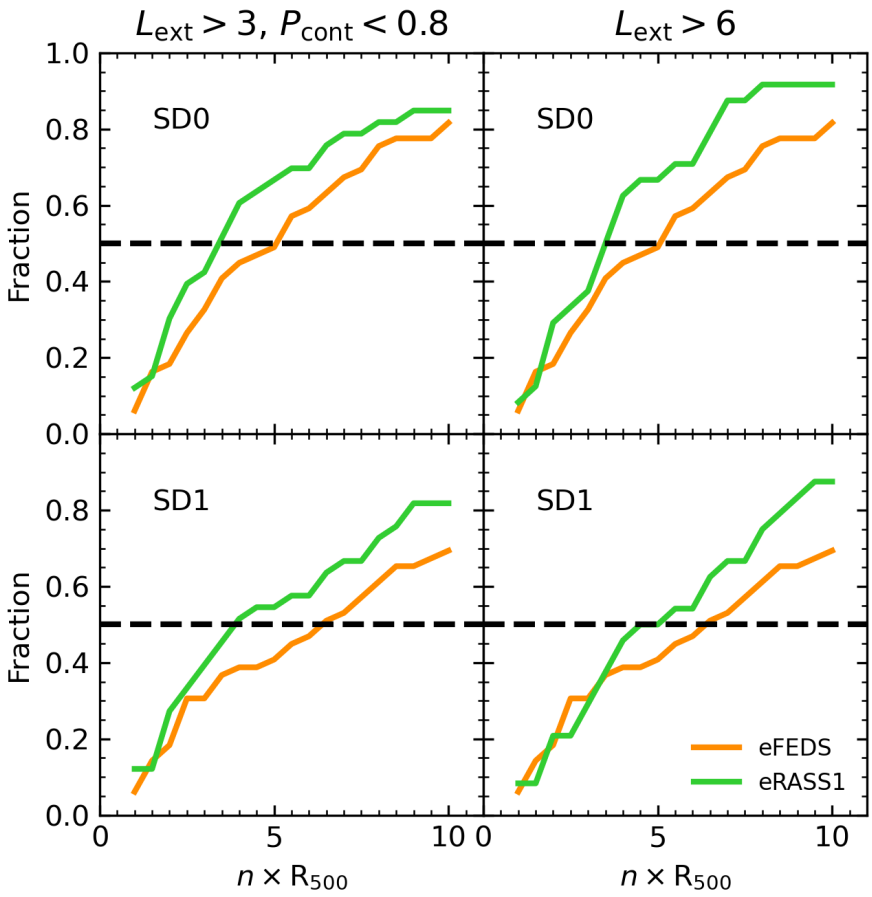


**Fig. 12** Fraction of clusters with at least one associated maximum within $n \times R_{500}$ as a function of $n$. The two columns refer to the different cluster samples (Large, left column and Pure, right column, respectively), while the two rows refer to the different smoothing levels (SD0, top row, and SD1, bottom row, respectively). The green line shows the fraction for the respective cluster sample. In each panel, the orange line shows the corresponding fraction for the eFEDS sample. These lines do not vary across columns. The black dashed line highlights a fraction of 50% for reference.

## 7.4 Comparing the DESI LS and GAMA

We also perform a comparison between 3D and 2D connectivity, multiplicity, and number of filament connections, using the 3D measurement performed in GAMA and the 2D measurement performed in the DESI LS, for the few clusters that have a connectivity measurement in both. Figure 15 shows an example of such a comparison for the connectivity, multiplicity, and filament connections for the Pure sample of the eRASS1 clusters. For each cluster with a 3D measurement of $\kappa$, $\mu$, or connections

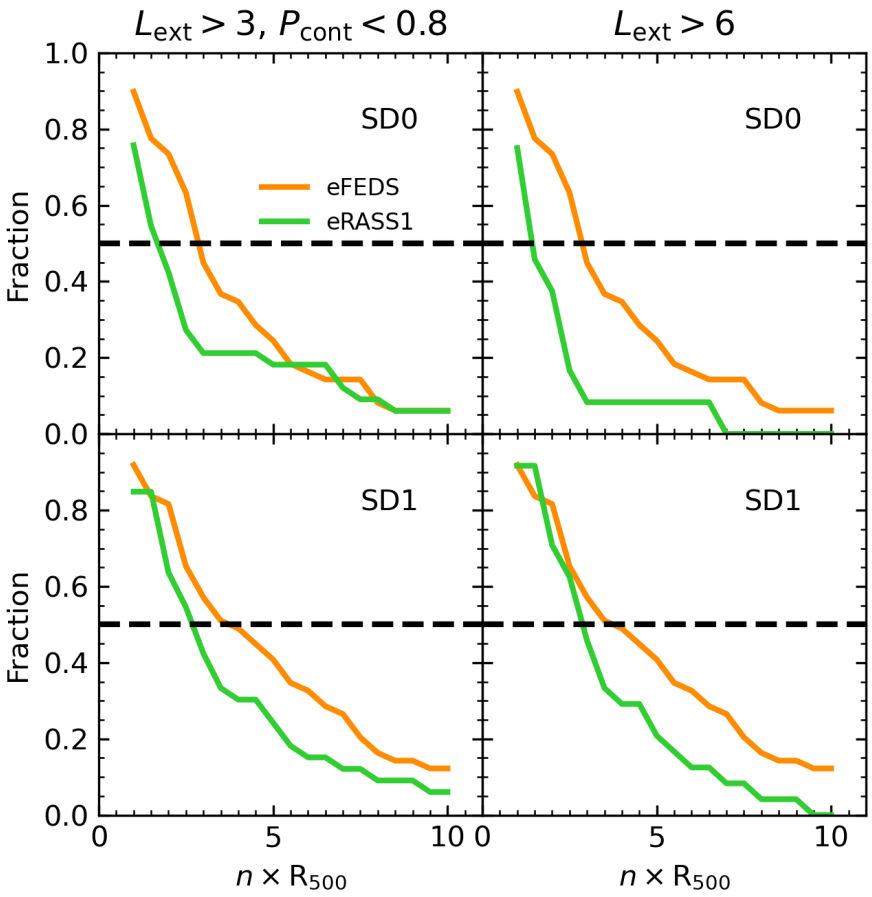


**Fig. 13** Fraction of clusters with no associated critical point within $n \times R_{500}$ as a function of $n$. The two columns refer to the different cluster samples (Large, left column and Pure, right column, respectively), while the two rows refer to the different smoothing levels (SD0, top row, and SD1, bottom row, respectively). The green line shows the fraction for the respective cluster sample. In each panel, the orange line shows the corresponding fraction for the eFEDS sample. These lines do not vary across columns. The black dashed line highlights a fraction of 50% for reference.

coming from the GAMA skeleton (both in the SD0 and SD1 case), we look for its 2D value of $\kappa$, $\mu$, or connections coming from the DESI LS skeleton (only in the SD0 case, for both the skeleton measured on the entire survey and the one extracted in the postage stamp case, with a $2\sigma$ persistence threshold).

We find that, as expected and demonstrated throughout this paper and Malavasi et al. (under review), the $\kappa$, $\mu$, and connections values derived in the DESI LS for the SD0 case are consistent with those derived in 3D for the SD1 case on the GAMA

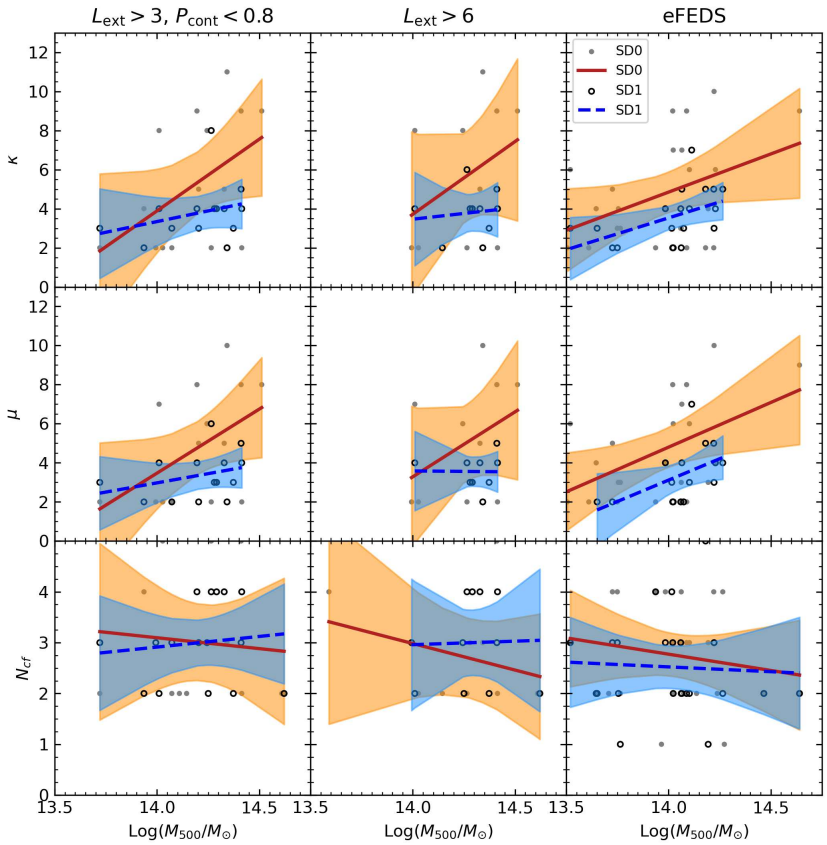


**Fig. 14** The connectivity-mass (top row), multiplicity-mass (middle row), and filament connections-mass (bottom row) relations for the eRASS1 Large (left column) and Pure (middle column) samples, and the eFEDS (right column) clusters, derived using the GAMA skeleton. In each panel, grey points and black circles refer to the individual measurements for the clusters (SD0 and SD1 cases, respectively, all three GAMA fields combined). The solid red line with orange shade corresponds to the linear fit for the SD0 case, the dashed blue line with light blue shade to the SD1 case.

skeleton. Measurements in this case are generally distributed along the 1:1 relation, albeit with a large scatter. In the case of a comparison between the DESI LS SD0 case and the GAMA SD0 case, we see that the $\kappa$, $\mu$, and connections values for GAMA are higher than those detected in the DESI LS.

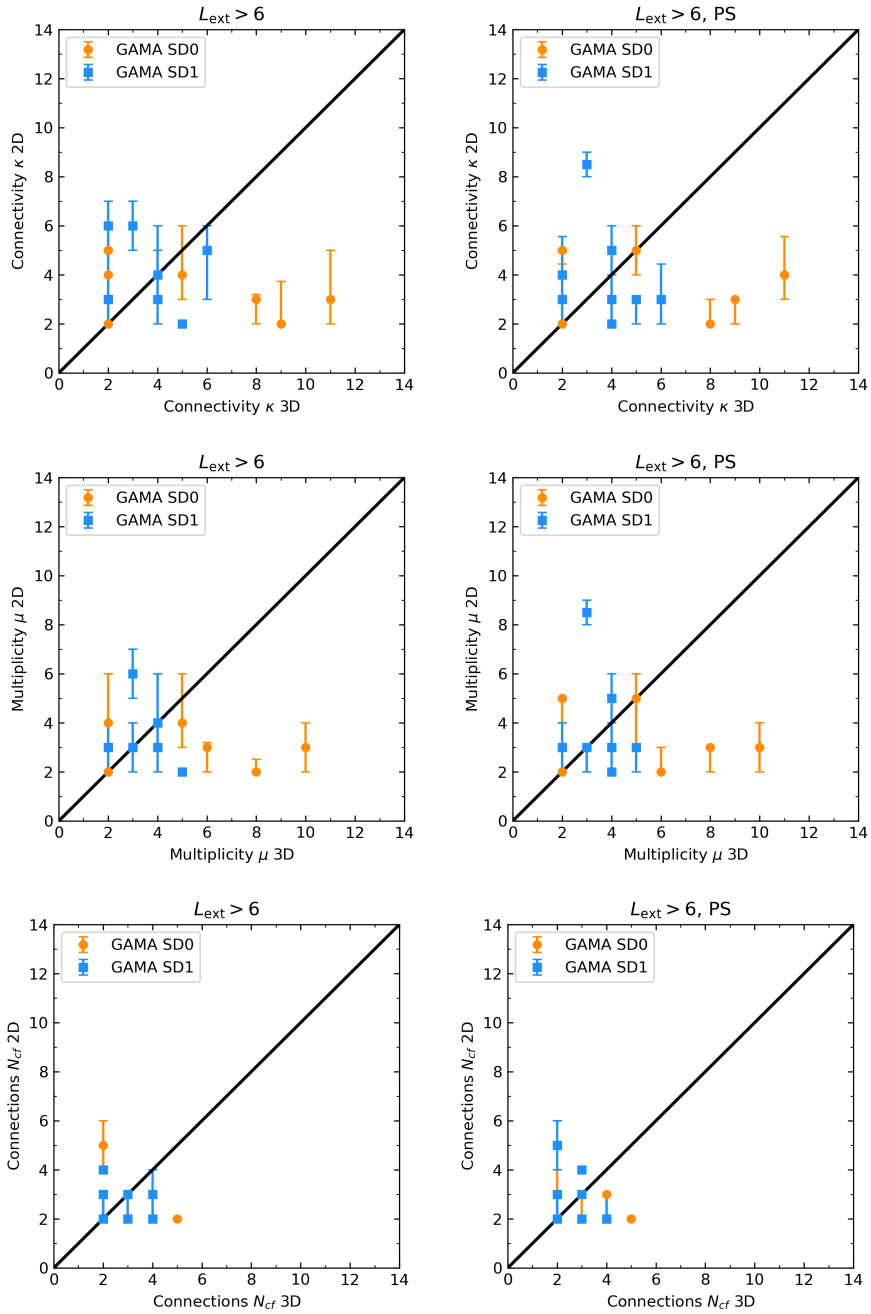


**Fig. 15** Comparison of 3D and 2D connectivity (top row), multiplicity (middle row), and filament connections (bottom row). Left column refers to the skeleton computed on the full survey volume, right column to the skeleton computed in the postage stamp case, both with a $2\sigma$ persistence threshold. In each panel, blue squares refer to the case where the DESI LS SD0 case is compared to the GAMA SD1 case, while the orange circles where it is compared to the GAMA SD0 case. The black diagonal line is the 1:1 relation, reported for reference.

# 8 Literature measurements of the $[\kappa, \mu, N_{cf}]$-mass relation

In this work we compare our results with several other analyses in the literature. We summarize in this section the main similarities and differences between the literature and the results of this work.

In particular we compare our analysis with the theoretical works of [18] (which performed a detection of the connectivity-mass relation in a dark matter only numerical simulation), [42] (who also detected filament connections in a dark matter only numerical simulation), [32] (which detected filament connections in the IllustrisTNG hydrodynamical simulation), [41] (which detected halo connectivity on the MillenniumTNG simulation) and [34] (which detected the connectivity-mass relation in The300 simulation). From the observational side, we compare ourselves with [19] and [22] (which detected the multiplicity-mass relation in the CFHTLS, and COSMOS surveys, respectively) and [24] which detected the multiplicity-mass relation in the Euclid Q1 data. We also compare our results with [26] and [30] (which detected the filament connections of the observed and simulated versions of the Coma cluster) and [43] (which detected the filament connections of A2744).

The main points to consider when comparing these works are: the redshift range explored, the type of redshifts used to extract the skeletons, the uncertainty on the redshift measurement, the mass range of the cluster sample explored, the algorithm used to extract the skeleton from the galaxy distribution, and the way in which connectivity, multiplicity, or filament connections have been measured. Table 2 summarizes the main similarities and differences between our work and the rest of the literature.

From this table it is possible to extract the following pieces of information. First of all, the DESI LS galaxies we use to extract the skeleton have worse photometric redshifts compared to Euclid, CFHTLS, and COSMOS. In particular, [19] cites an average photometric redshift uncertainty of 0.03 for their work and of 0.008 for [22], who state that the photo-z uncertainty for their lower mass galaxies (that have the largest uncertainties on photo-zs) is of 0.035. [57] cite photometric redshift uncertainties in the range 0.03-0.07 for the galaxy sample used by [24], depending on the magnitude cut applied to the sample. Despite this, we are still able to detect a meaningful connectivity-mass relation.

There is a large agreement in the mass range of the clusters analyzed, if we exclude [22] who explored groups and reach much smaller masses than this study. At the same time, there is not a good overlap in terms of redshift ranges explored, with the majority of the works focusing on higher redshifts than this work. We are therefore unable to constrain how much the differences between our work and the literature are due to a possible trend in the connectivity-mass relation with redshift.

In general, all works explore connectivity, multiplicity, and connections at a certain distance from clusters, with the choice of the distance largely varying. It is possible that the choice of the scale does not have a too strong of an impact, given the agreement between all of these works.

We are also aware of other works that explored the connections to the filaments of the cosmic web of large structures (superclusters, see, e.g., [27], [58], [31]). However,

**Table 2** TBD

| Ref. | $\Delta z$ | $\sigma_{z/(1+z)}$ | $\Delta M\,(M_\odot)$ | Algorithm | Quantity/Scale |
|---|---|---|---|---|---|
| [42] | $z = 0$ | - | $M_{\rm vir}$[1] $\geq 10^{14}\,h^{-1}$ | MMF | Connections[2]/3 Mpc $h^{-1}$ |
| [19] | $0.15 \leq z \leq 0.7$ | 0.03 | $M_{200} \geq 10^{14}$ | DisPerSE[3] | Multiplicity[4,5]/1.5 cMpc |
| [22] | $0.5 \leq z \leq 1.2$ | 0.008-0.035 | $M_{200}$[6] $\geq 10^{13.38}$ | DisPerSE[3] | Multiplicity[5]/1.5 $\times$ $R_{\rm vir}$[5] |
| [18] | $z = 0$ | - | $M_{\rm vir}$[1] $\geq 7.7 \times 10^{11}$ | DisPerSE | Connectivity[7] |
| [26] | $z = 0.023$ | - | $M_{200} = 5.3 \times 10^{14}$ | DisPerSE | Connections/1.5 $\times$ $R_{\rm vir}$[5] |
| [32] | $z = 0$ | - | $M_{200} \geq 10^{13}\,h^{-1}$ | T-ReX | Connections[8,5]/1.5 $\times$ $R_{200}$ |
| [30] | $z = 0$ | - | $M_{200} = 9.441 \times 10^{14}\,h^{-1}$ | DisPerSE | Connections/1.5 $\times$ $R_{\rm vir}$[5] |
| [34] | $0 \leq z \leq 2$ | - | $10^{13} \leq M_{200}(h^{-1}) \leq 2.62 \times 10^{15}$ | DisPerSE[9] | Connectivity[10,11]/$R_{500}$, $R_{200}$, $R_{\rm vir}$ |
| [41] | $0 \leq z \leq 4$ | - | $M_{200} \geq 5 \times 10^{11}\,h^{-1}$ | DisPerSE | Connectivity[11,12]/1.5 $\times$ $R_{200}$ |
| [43] | $z = 0.306$ | - | $M_{200} = 2 \times 10^{15}$ | T-Rex[11] | Connections |
| [24] | $0.2 \leq z \leq 0.7$ | 0.03-0.07 | $10^{13.5} \leq M_{500} \leq 10^{15}$ | DisPerSE and T-ReX[13] | Multiplicity/2, 3, 4 $\times$ $R_{500}$ |
| This work - GAMA | $0.03 \leq z \leq 0.25$ | - | $10^{13.5} \leq M_{500} \leq 10^{15}$ | DisPerSE | All/adaptive scale |
| This work - DESI LS | $0.03 \leq z \leq 0.4$ | 0.052 | $10^{13.5} \leq M_{500} \leq 10^{15}$ | DisPerSE | All/adaptive scale |

[1] Although it is never explicitly mentioned in the text, the mass recovered by the halo finder used should be akin to virial mass.

[2] A filament is considered connected to a cluster if a halo belonging to the filament is within 3 Mpc $h^{-1}$ of the cluster center.

[3] Run in 2D on full survey area, in redshift slices centered at the redshift of each cluster.

[4] A cluster is matched to its closest node. If no node is found within $R_{200}$ from cluster center, then the cluster is unmatched.

[5] Only filaments crossing a sphere of radius equal to the mentioned scale are counted.

[6] However, as [22] uses a group sample, their most massive object has a mass $M_{200} < 10^{14.5} M_\odot$

[7] Haloes are matched to their closest node. All filaments attached to the node are counted.

[8] Clusters are matched to their closest node. If the closest node is $> 1{\rm Mpc}\,h^{-1}$ away from the cluster, it is discarded.

[9] Run directly on the gas particles.

[10] All filaments originating from critical points within the chosen radius are considered, only those crossing a sphere of given radius are counted. In this work we compare with the connectivity-mass relation of [34] measured using $R_{200}$.

[11] We only compare with the measurement performed at $z = 0$.

[12] The DisPerSE parameters are tuned to maximize the match between haloes and maxima. A halo is considered matched to a given maximum if it is located within the halo $R_{200}$.

[13] Both methods are run in 2D on the full survey area, in redshift slices centered at the redshift of each cluster. In this work we compare only with the multiplicity-mass relation extracted using DisPerSE.

the complexity of the structures that they analyze makes it difficult to report them on the connectivity-mass plane for a fair comparison. In the same way, works exploring the scale of galaxies (see, e.g., [59] and [60]) explore a different class of objects and are therefore not reported here.

# 9 Further systematic checks

## 9.1 Multiplicity-mass relation

In this subsection we present, for completeness, the multiplicity-mass relation for the DESI LS skeleton extracted in the full survey footprint with a persistence threshold of $2\sigma$ (Figure 16).

As is the case with connectivity (expected, given the strong link between the two), multiplicity also presents a positive correlation with mass, which we fit using Equations (4) and (5). This relation is visible up to redshift $z \sim 0.27$.

## 9.2 Full survey skeleton extraction, higher persistence thresold

We report in this section the results that we obtain if we increase the persistence threshold of the skeleton extraction performed in the full survey footprint to $3\sigma$. Figures 17 and 18 show renditions of Figures 7 and 8 obtained with a persistence threshold of $3\sigma$.

From these figures it is possible to see how the matching of critical points to eRASS1 clusters is more complicated in the $3\sigma$ persistence case. In the SD0 case, intermediate redshift slices have a fraction of clusters with at least one associated maximum within $n \times R_{500}$ above 50% at factors $n \geq 5$. Conversely, the fraction of clusters with no associated critical point is below 50% only at values of $n \geq 3$. In the case of SD1 both fractions are consistently above or below 50%, which forces us to discard this skeleton realization.

Figures 19 and 20 show renditions of Figures 1 and 2 made with a persistence threshold of $3\sigma$. They clearly show that both a connectivity-mass and a filament connections-mass relation can be detected also with a higher persistence threshold (albeit with a shallower slope) and that the filament connections-mass relation is difficult to recover, with a very shallow slope at all redshifts.

## 9.3 Postage stamp skeleton extraction

In the case of the DESI LS skeleton built with the postage stamp technique we proceed in the same way as with the skeleton extracted on the full area. For each cluster we look for maxima and other critical points located within each cluster's $n \times R_{500}$. We repeat the association for each of the 100 extractions. We do it individually for each cluster. However, as the rest of the analysis is then performed in the redshift slices introduced above, we bin the clusters in the same redshift slices.

The postage stamp skeleton extraction presents an improved situation with respect to the skeleton extracted in the full survey area with the $3\sigma$ persistence threshold case similar to the $2\sigma$ case. In the case of maxima associated to clusters, the value of $n_\kappa$ for which more than 50% of clusters have their closest maximum within $n_\kappa \times R_{500}$ is

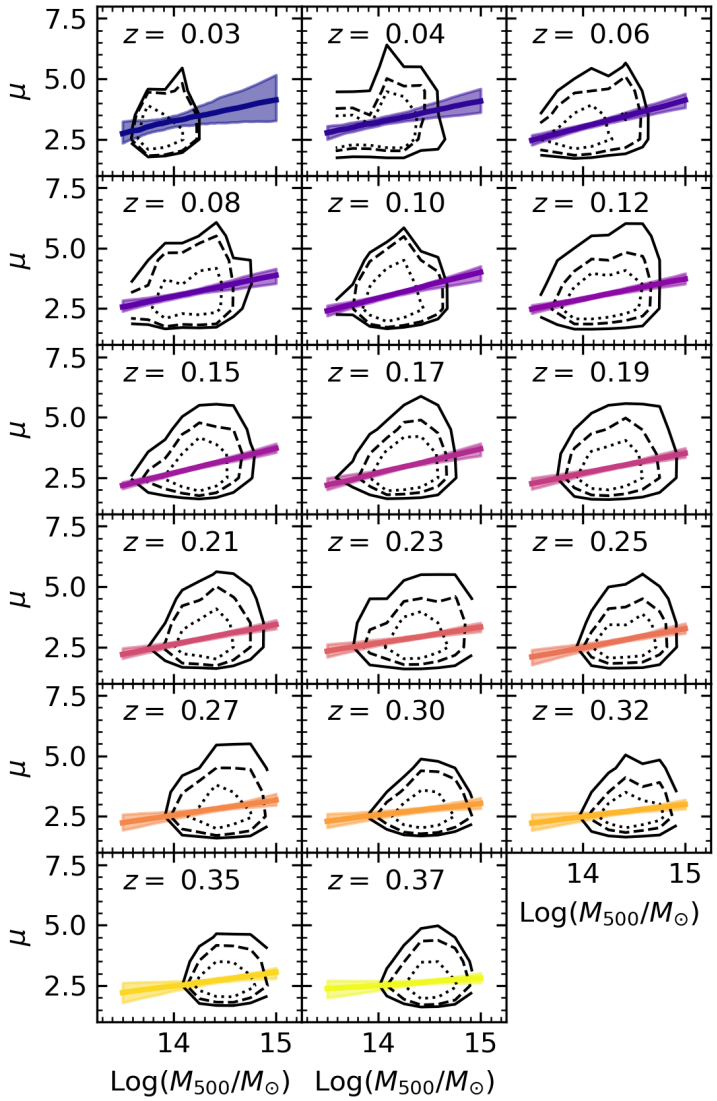


**Fig. 16** The multiplicity-mass relation for eRASS1 clusters. In each panel we show a different redshift slice, as marked in the corner. Black contours show the location of the data points (the solid line encircles 90% of the data, the dashed line 75%, and the dotted line 50%). They were derived as the median values of the same contours across the 100 Montecarlo extractions. The line in each panel represents the linear fit to the data, color-coded according to redshift. The line is the median of the individual fits of the 100 Montecarlo extractions. The shaded region shows the range encompassing 68% of the extractions. Only the SD0 case for the Pure cluster sample is shown. The persistence threshold is set to $2\sigma$.

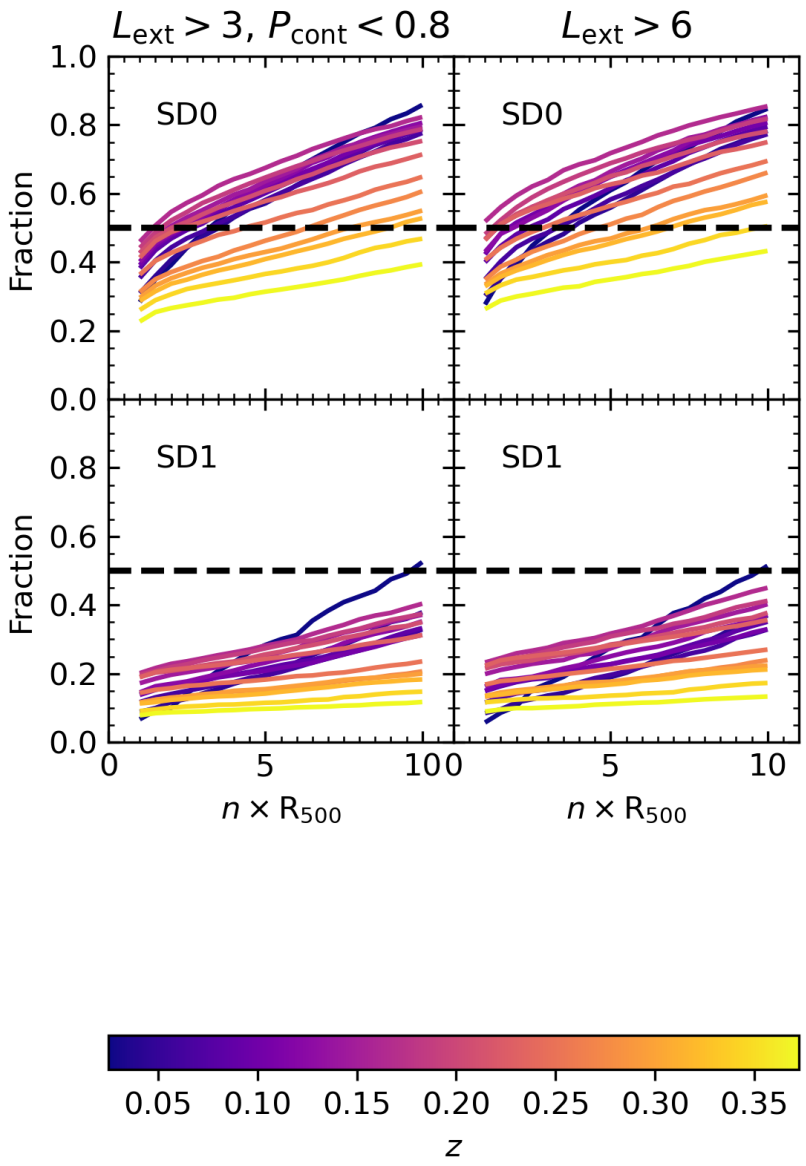


**Fig. 17** Same as Figure 7 but for the skeleton extracted in the full survey volume with a persistence of $3\sigma$.

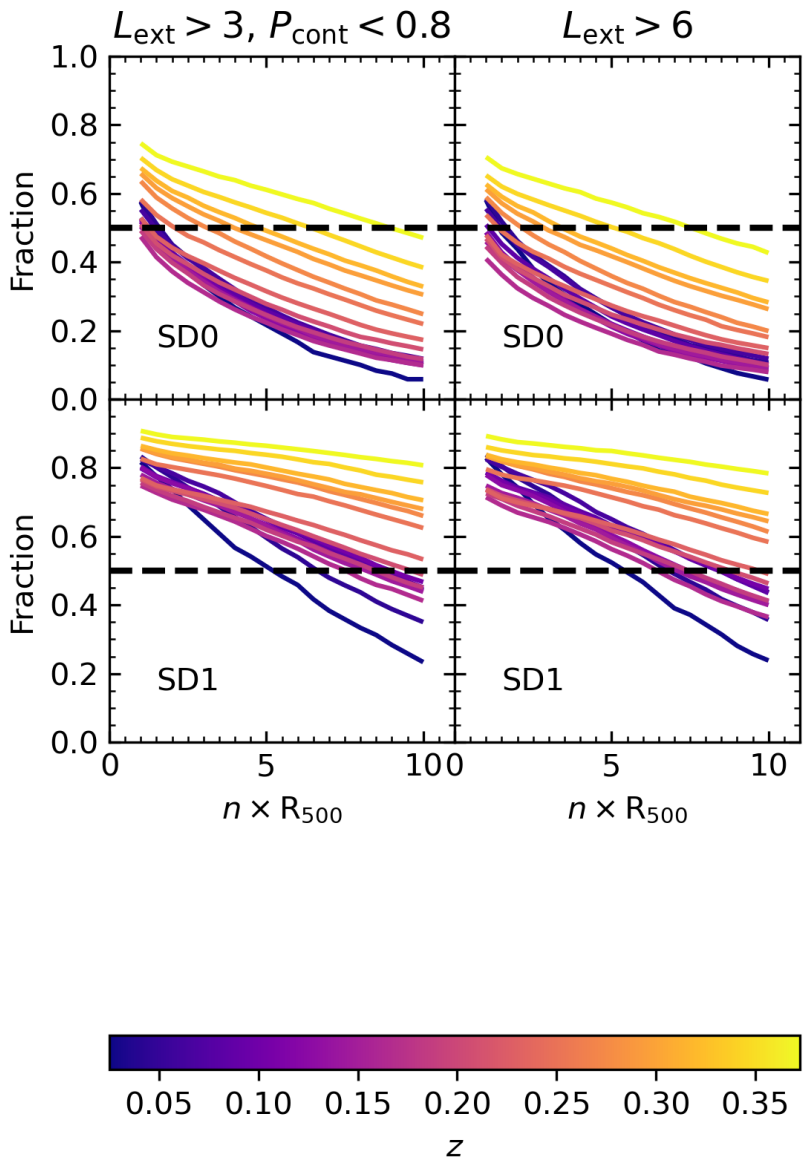


**Fig. 18** Same as Figure 8 but for the skeleton extracted in the full survey volume with a persistence of $3\sigma$.

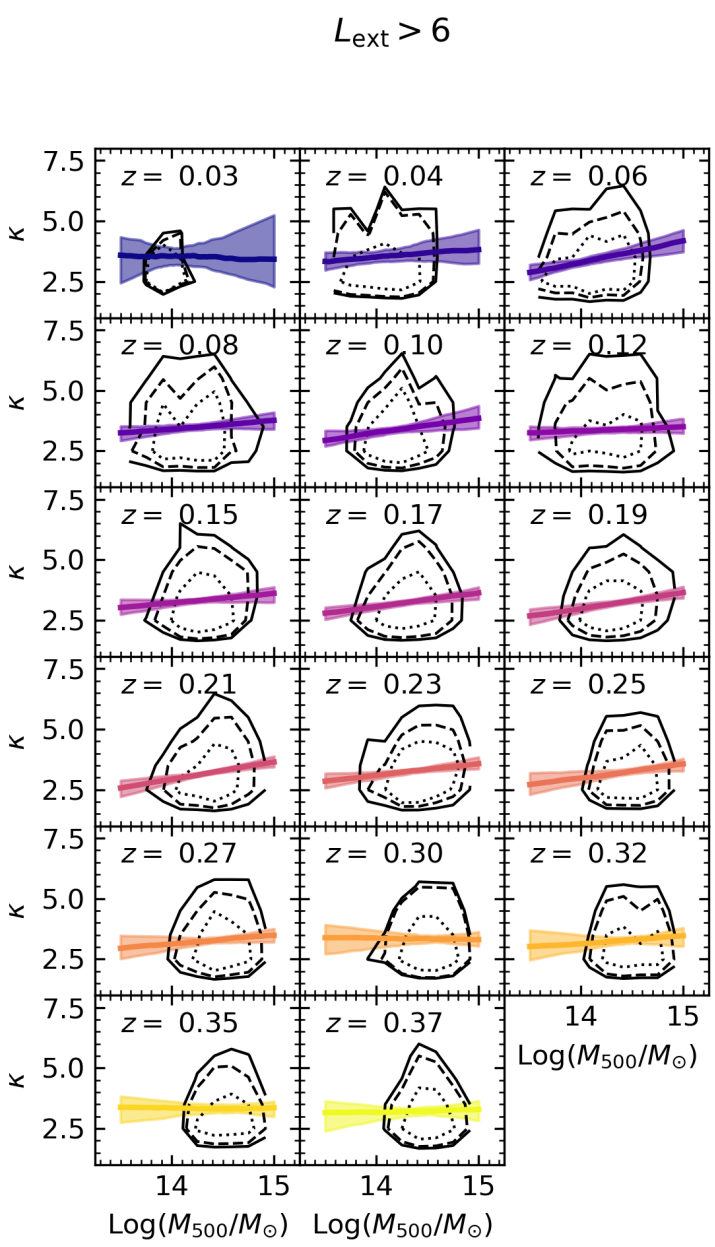


**Fig. 19** Same as Figure 1 but for the skeleton extracted in the full survey volume with a persistence of $3\sigma$.

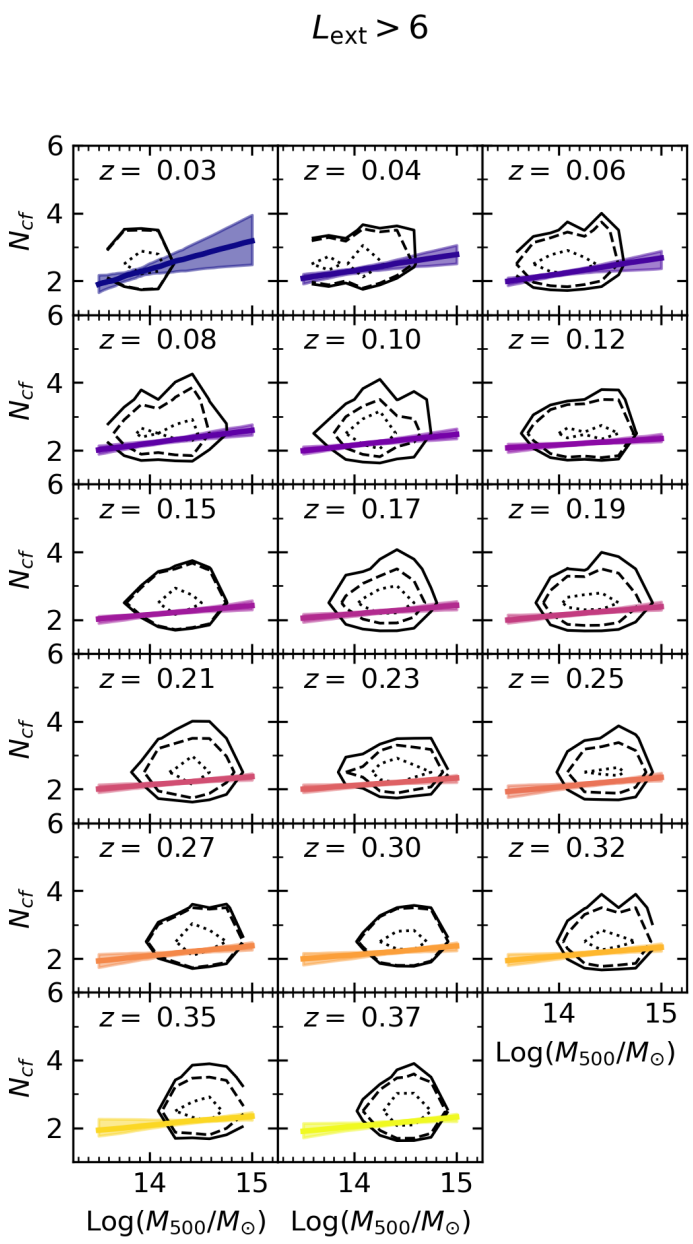


**Fig. 20** Same as Figure 2 but for the skeleton extracted in the full survey volume with a persistence of $3\sigma$.

smaller than in the case where the skeleton is extracted over the full sky area with a $3\sigma$ persistence threshold. All redshift slices now have also fractions above 30%. Moreover, the fraction of clusters with no critical point identified within $R_{500}$ drops from $\sim 80\%$ to $\sim 60\%$ in the case of SD0 for the Large sample. This is shown in Figures 21 and 22 (for a $2\sigma$ persistence threshold) and in Figures 23 and 24 (for a $3\sigma$ persistence threshold). As it was the case for the full survey footprint, the matching of DisPerSE output to the eRASS1 clusters performs better in the case of a $2\sigma$ persistence threshold (results presented in the rest of the paper use this value), but the same results can be achieved with $3\sigma$ too. In the postage stamp skeleton case too, the performance of the SD1 case is judged insufficient, especially when the $3\sigma$ threshold is applied, and therefore excluded from the rest of the analysis (the fraction of clusters with at least one associated maximum is below 50% even within $10R_{500}$ at all redshifts, while the fraction of clusters with no critical points reaches below 50% for values of $n_{\rm fc} = 5$ at all redshifts).

Finally, Figures 25, 26, and 27 show the connectivity-mass, multiplicity-mass, and filament connections-mass relations in the case of the postage stamp skeleton extraction with a $2\sigma$ persistence threshold. In these figures too we report only the SD0 case.

In the case of the postage stamp skeleton we observe a strong relationship with mass for all quantities considered (connectivity, multiplicity, and filament connections). The slopes of the linear fits are steep and the relations can still be seen up to $z = 0.27$. In this case the connectivity-mass relation is clearly detected and present for the cluster sample we analyze.

**Acknowledgements.** Nicola Malavasi acknowledges funding by the European Union through a Marie Skłodowska-Curie Action Postdoctoral Fellowship (Grant Agreement: 101061448, project: MEMORY). Views and opinions expressed are however those of the author only and do not necessarily reflect those of the European Union or of the Research Executive Agency. Neither the European Union nor the granting authority can be held responsible for them.

# References

[1] Gregory, S.A., Thompson, L.A., Tifft, W.G.: The Perseus/Pisces Supercluster. In: Bulletin of the American Astronomical Society, vol. 10, p. 622 (1978)

[2] Jõeveer, M., Einasto, J., Tago, E.: Spatial distribution of galaxies and of clusters of galaxies in the southern galactic hemisphere. MNRAS **185**, 357–370 (1978) https://doi.org/10.1093/mnras/185.2.357

[3] de Lapparent, V., Geller, M.J., Huchra, J.P.: A Slice of the Universe. ApJL **302**, 1 (1986) https://doi.org/10.1086/184625

[4] Giovanelli, R., Haynes, M.P., Chincarini, G.L.: Morphological Segregation in the Pisces-Perseus Supercluster. ApJ **300**, 77 (1986) https://doi.org/10.1086/163784

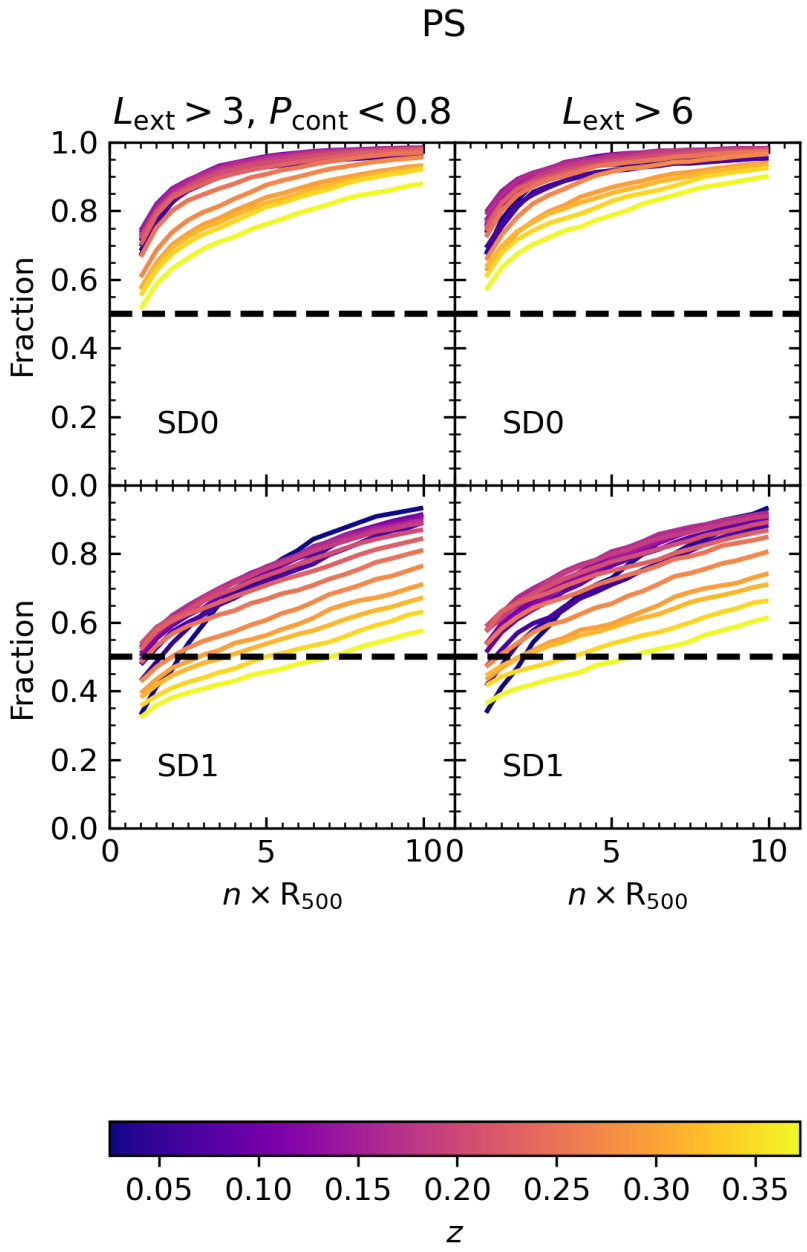


**Fig. 21** Same as Figure 7 but for the skeleton extracted with the postage stamp technique with a persistence of $2\sigma$.

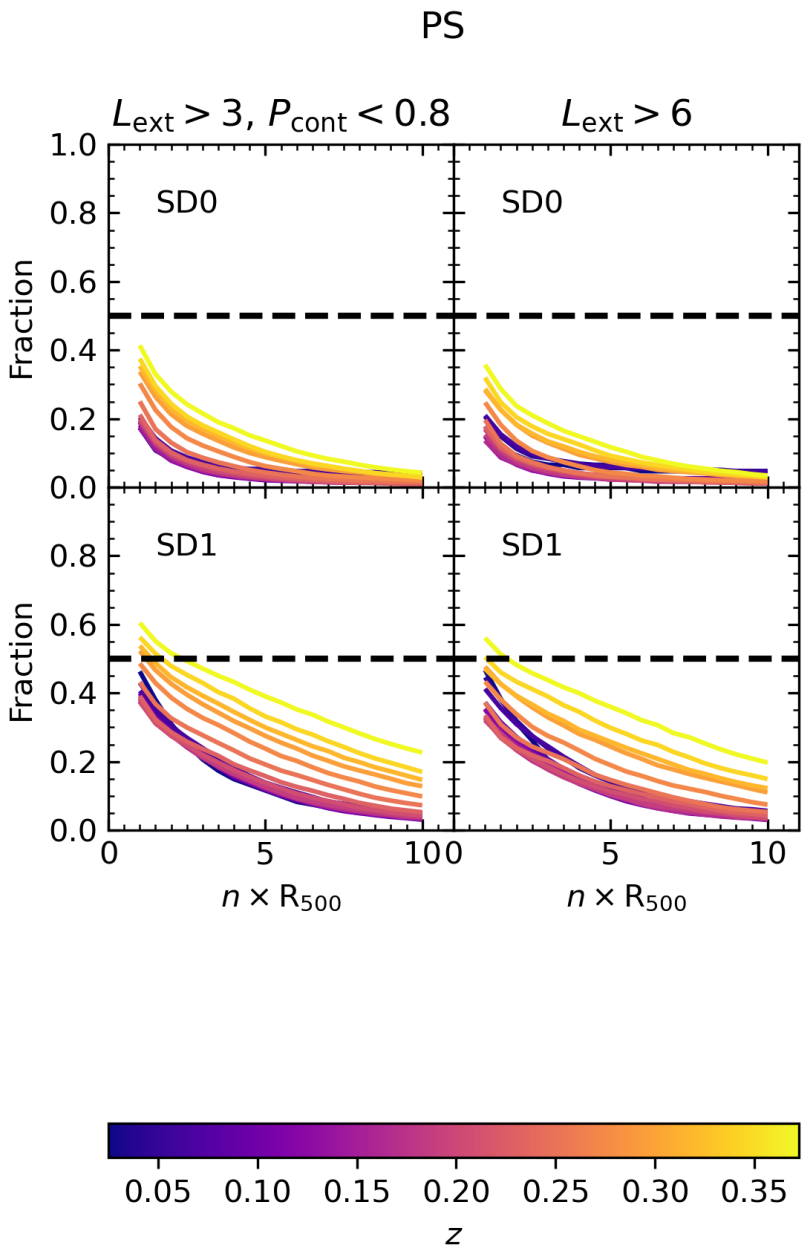


**Fig. 22** Same as Figure 8 but for the skeleton extracted with the postage stamp technique with a persistence of $2\sigma$.

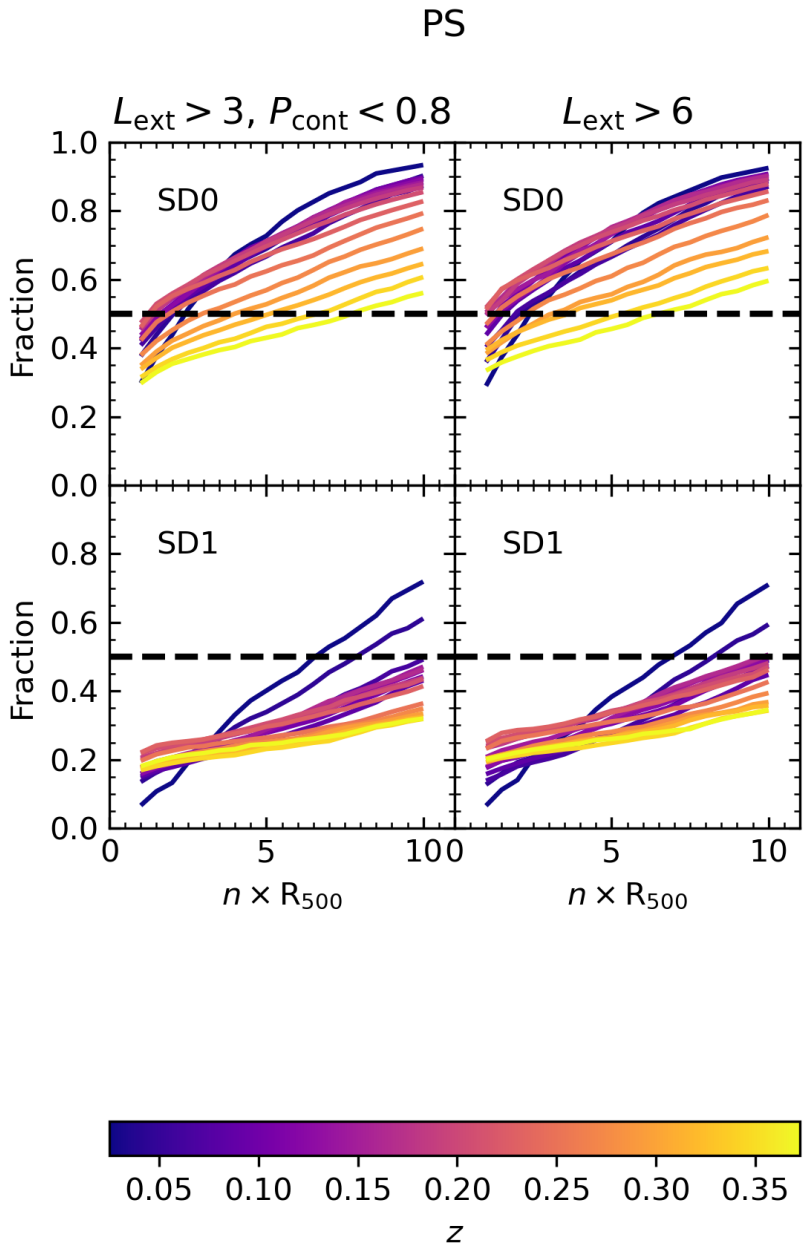


**Fig. 23** Same as Figure 21 but for the skeleton extracted with the postage stamp technique with a persistence of $3\sigma$.

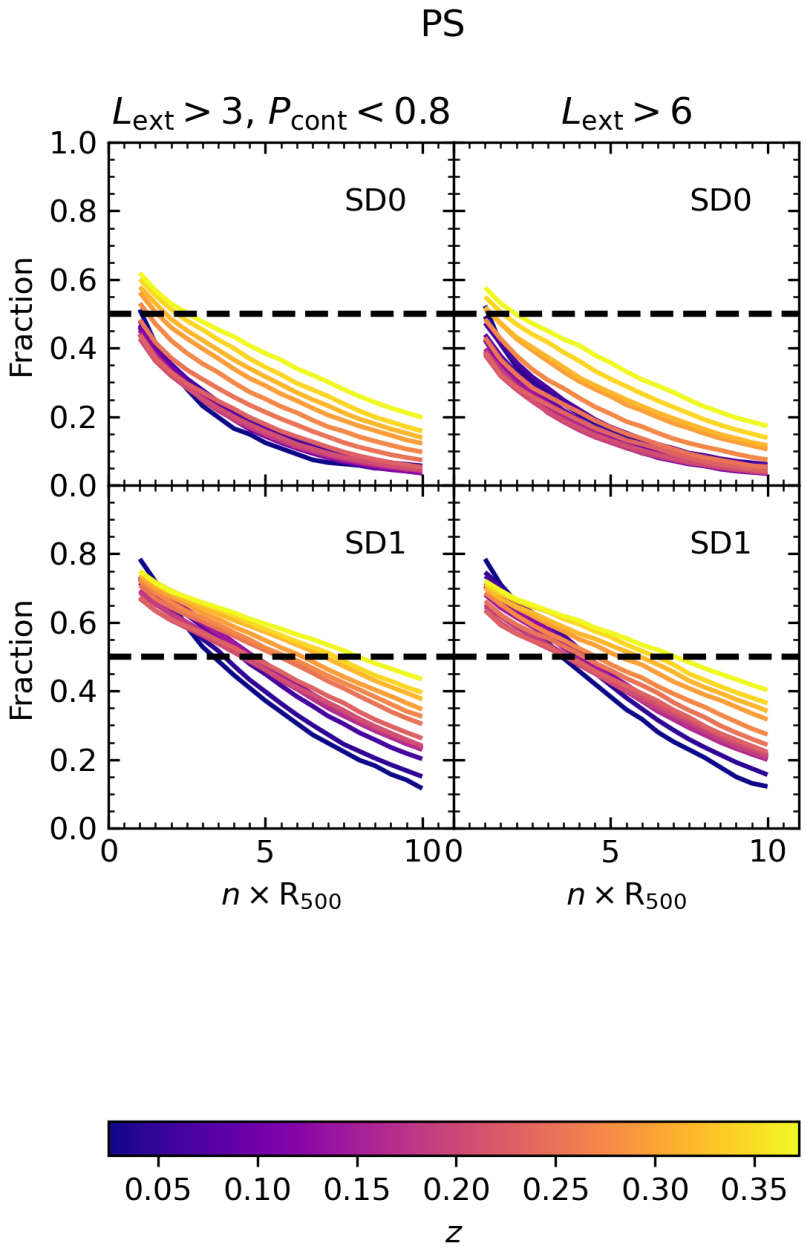


**Fig. 24** Same as Figure 22 but for the skeleton extracted with the postage stamp technique with a persistence of $3\sigma$.

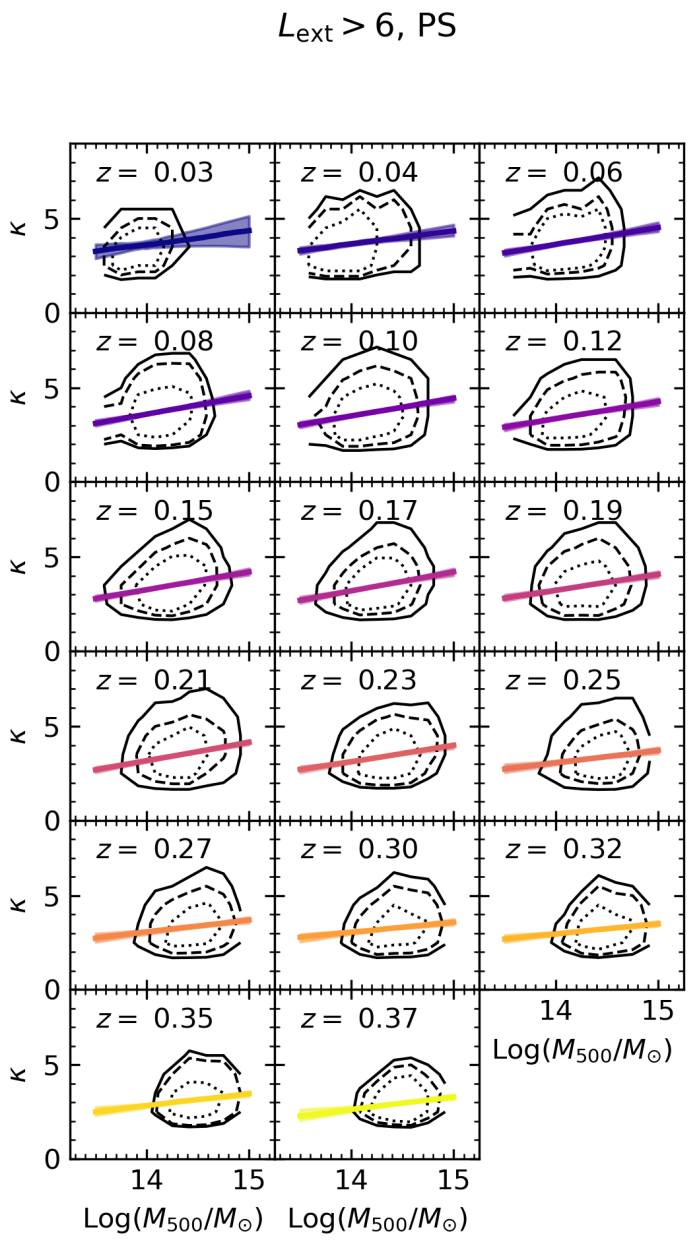


**Fig. 25** Same as Figure 1 but for the skeleton extracted with the postage stamp technique with a persistence of $2\sigma$.

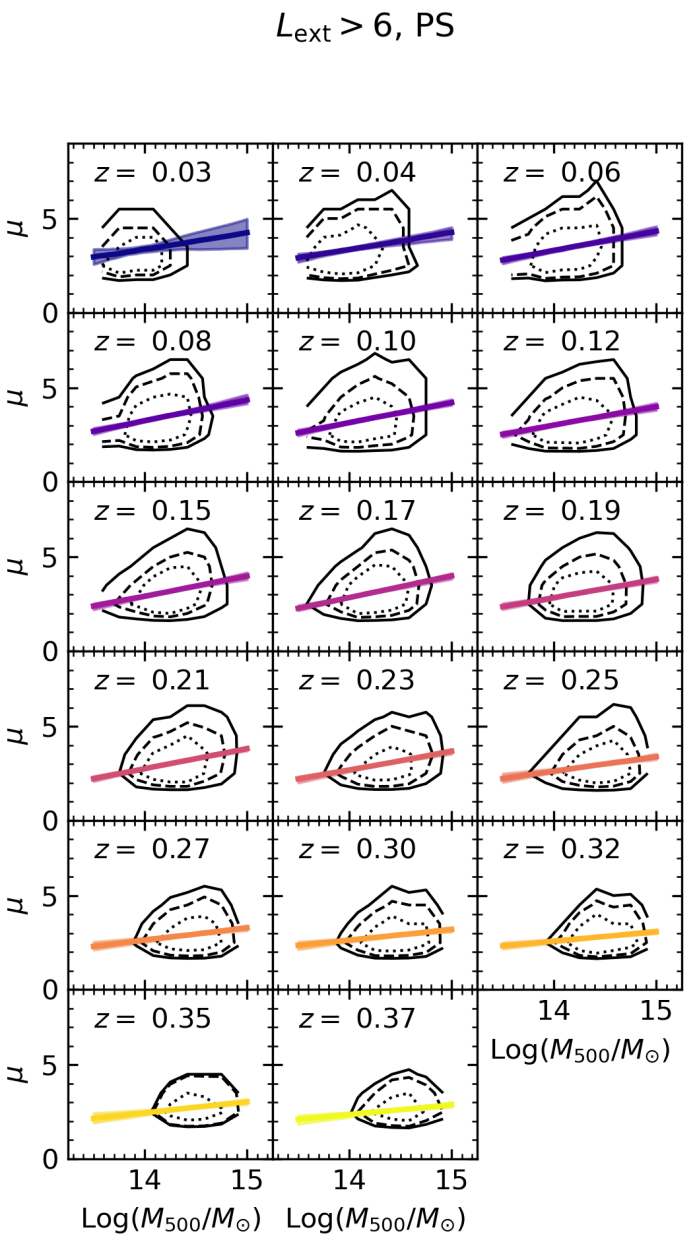


**Fig. 26** Same as Figure 25 but for the multiplicity-mass relation.

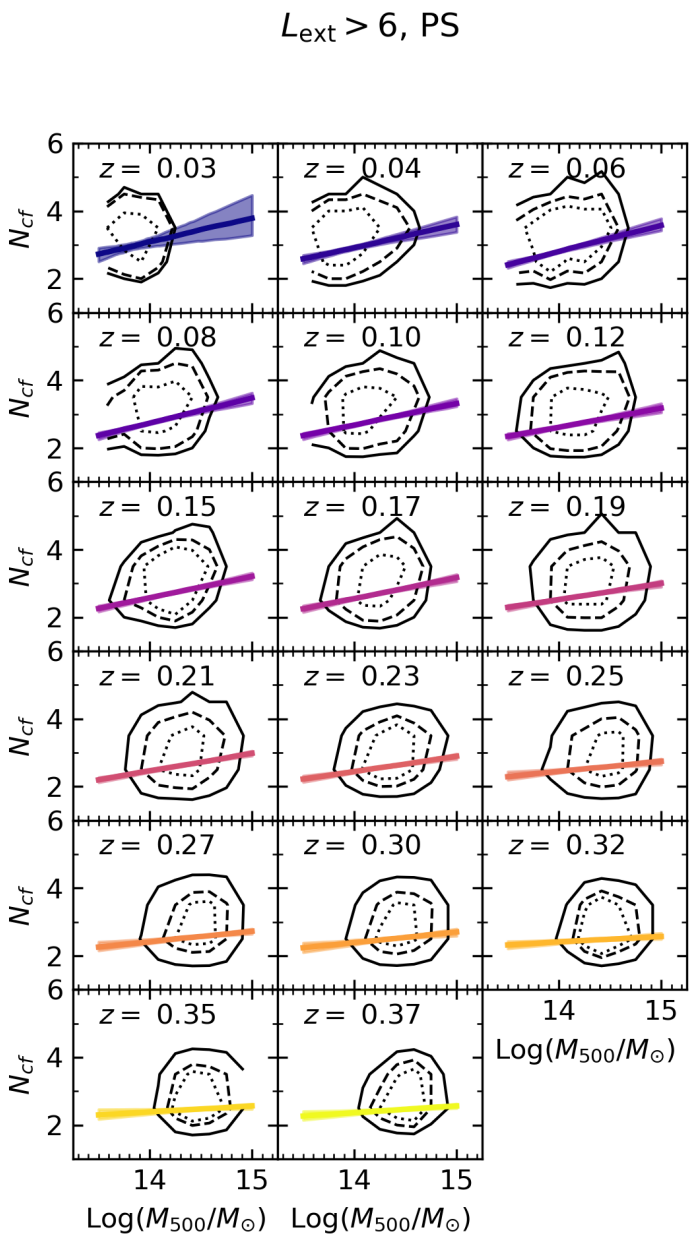


**Fig. 27** Same as Figure 25 but for the filament connections-mass relation.

[5] Geller, M.J., Huchra, J.P.: Mapping the Universe. Science **246**(4932), 897–903 (1989) https://doi.org/10.1126/science.246.4932.897

[6] Shectman, S.A., Landy, S.D., Oemler, A., Tucker, D.L., Lin, H., Kirshner, R.P., Schechter, P.L.: The Las Campanas Redshift Survey. ApJ **470**, 172 (1996) https://doi.org/10.1086/177858 arXiv:astro-ph/9604167 [astro-ph]

[7] Bond, J.R., Kofman, L., Pogosyan, D.: How filaments of galaxies are woven into the cosmic web. Nature **380**(6575), 603–606 (1996) https://doi.org/10.1038/380603a0 arXiv:astro-ph/9512141 [astro-ph]

[8] Feldbrugge, J., van de Weygaert, R., Hidding, J., Feldbrugge, J.: Caustic Skeleton & Cosmic Web. JCAP **2018**(5), 027 (2018) https://doi.org/10.1088/1475-7516/2018/05/027 arXiv:1703.09598 [astro-ph.CO]

[9] Feldbrugge, J., van de Weygaert, R.: What makes a cosmic filament? The dynamical origin and identity of filaments – I. Fundamentals in 2D. MNRAS **539**(2), 873–901 (2025) https://doi.org/10.1093/mnras/staf536 arXiv:2405.20475 [astro-ph.CO]

[10] Dekel, A., Birnboim, Y., Engel, G., Freundlich, J., Goerdt, T., Mumcuoglu, M., Neistein, E., Pichon, C., Teyssier, R., Zinger, E.: Cold streams in early massive hot haloes as the main mode of galaxy formation. Nature **457**(7228), 451–454 (2009) https://doi.org/10.1038/nature07648 arXiv:0808.0553 [astro-ph]

[11] Dekel, A., Birnboim, Y.: Galaxy bimodality due to cold flows and shock heating. MNRAS **368**(1), 2–20 (2006) https://doi.org/10.1111/j.1365-2966.2006.10145.x arXiv:astro-ph/0412300 [astro-ph]

[12] Overzier, R.A.: The realm of the galaxy protoclusters. A review. A&ApR **24**(1), 14 (2016) https://doi.org/10.1007/s00159-016-0100-3 arXiv:1610.05201 [astro-ph.GA]

[13] Danovich, M., Dekel, A., Hahn, O., Teyssier, R.: Coplanar streams, pancakes and angular-momentum exchange in high-z disc galaxies. MNRAS **422**(2), 1732–1749 (2012) https://doi.org/10.1111/j.1365-2966.2012.20751.x arXiv:1110.6209 [astro-ph.CO]

[14] Aragon Calvo, M.A., Neyrinck, M.C., Silk, J.: Galaxy Quenching from Cosmic Web Detachment. The Open Journal of Astrophysics **2**(1), 7 (2019) https://doi.org/10.21105/astro.1697.07881 arXiv:1607.07881 [astro-ph.GA]

[15] Bennett, J.S., Sijacki, D.: Resolving shocks and filaments in galaxy formation simulations: effects on gas properties and star formation in the circumgalactic medium. MNRAS **499**(1), 597–615 (2020) https://doi.org/10.1093/mnras/staa2835 arXiv:2006.10058 [astro-ph.GA]

[16] Valentini, M., Gallerani, S., Ferrara, A.: Host galaxies of high-redshift quasars: SMBH growth and feedback. MNRAS **507**(1), 1–26 (2021) https://doi.org/10.1093/mnras/stab1992 arXiv:2107.05638 [astro-ph.GA]

[17] Ramsøy, M., Slyz, A., Devriendt, J., Laigle, C., Dubois, Y.: Rivers of gas - I. Unveiling the properties of high redshift filaments. MNRAS **502**(1), 351–368 (2021) https://doi.org/10.1093/mnras/stab015 arXiv:2101.00844 [astro-ph.GA]

[18] Codis, S., Pogosyan, D., Pichon, C.: On the connectivity of the cosmic web: theory and implications for cosmology and galaxy formation. MNRAS **479**(1), 973–993 (2018) https://doi.org/10.1093/mnras/sty1643 arXiv:1803.11477 [astro-ph.CO]

[19] Sarron, F., Adami, C., Durret, F., Laigle, C.: Pre-processing of galaxies in cosmic filaments around AMASCFI clusters in the CFHTLS. A&A **632**, 49 (2019) https://doi.org/10.1051/0004-6361/201935394 arXiv:1903.02879 [astro-ph.GA]

[20] Coupon, J., Ilbert, O., Kilbinger, M., McCracken, H.J., Mellier, Y., Arnouts, S., Bertin, E., Hudelot, P., Schultheis, M., Le Fèvre, O., Le Brun, V., Guzzo, L., Bardelli, S., Zucca, E., Bolzonella, M., Garilli, B., Zamorani, G., Zanichelli, A., Tresse, L., Aussel, H.: Photometric redshifts for the CFHTLS T0004 deep and wide fields. A&A **500**(3), 981–998 (2009) https://doi.org/10.1051/0004-6361/200811413 arXiv:0811.3326 [astro-ph]

[21] Sarron, F., Martinet, N., Durret, F., Adami, C.: Evolution of the cluster optical galaxy luminosity function in the CFHTLS: breaking the degeneracy between mass and redshift. A&A **613**, 67 (2018) https://doi.org/10.1051/0004-6361/201731981 arXiv:1712.09481 [astro-ph.GA]

[22] Darragh Ford, E., Laigle, C., Gozaliasl, G., Pichon, C., Devriendt, J., Slyz, A., Arnouts, S., Dubois, Y., Finoguenov, A., Griffiths, R., Kraljic, K., Pan, H., Peirani, S., Sarron, F.: Group connectivity in COSMOS: a tracer of mass assembly history. MNRAS **489**(4), 5695–5708 (2019) https://doi.org/10.1093/mnras/stz2490 arXiv:1904.11859 [astro-ph.GA]

[23] Laigle, C., McCracken, H.J., Ilbert, O., Hsieh, B.C., Davidzon, I., Capak, P., Hasinger, G., Silverman, J.D., Pichon, C., Coupon, J., Aussel, H., Le Borgne, D., Caputi, K., Cassata, P., Chang, Y.-Y., Civano, F., Dunlop, J., Fynbo, J., Kartaltepe, J.S., Koekemoer, A., Le Fèvre, O., Le Floc'h, E., Leauthaud, A., Lilly, S., Lin, L., Marchesi, S., Milvang-Jensen, B., Salvato, M., Sanders, D.B., Scoville, N., Smolcic, V., Stockmann, M., Taniguchi, Y., Tasca, L., Toft, S., Vaccari, M., Zabl, J.: The COSMOS2015 Catalog: Exploring the 1 ¡ z ¡ 6 Universe with Half a Million Galaxies. ApJs **224**(2), 24 (2016) https://doi.org/10.3847/0067-0049/224/2/24 arXiv:1604.02350 [astro-ph.GA]

[24] Euclid Collaboration: Gouin, C., Laigle, C., Sarron, F., Bonnaire, T., Sorce, J.G., Aghanim, N., Magliocchetti, M., Quilley, L., Boldrini, P., Durret, F., Pichon, C., Kuchner, U., Malavasi, N., Kraljic, K., Gavazzi, R., Kang, Y.,

Stanford, S.A., Awad, P., Altieri, B., Amara, A., Andreon, S., Auricchio, N., Aussel, H., Baccigalupi, C., Baldi, M., Balestra, A., Bardelli, S., Basset, A., Battaglia, P., Bernardeau, F., Biviano, A., Bonchi, A., Branchini, E., Brescia, M., Brinchmann, J., Camera, S., Cañas-Herrera, G., Capobianco, V., Carbone, C., Carretero, J., Castellano, M., Castignani, G., Cavuoti, S., Chambers, K.C., Cimatti, A., Colodro-Conde, C., Congedo, G., Conselice, C.J., Conversi, L., Copin, Y., Courbin, F., Courtois, H.M., Cropper, M., Da Silva, A., Degaudenzi, H., de la Torre, S., De Lucia, G., Di Giorgio, A.M., Dolding, C., Dole, H., Dubath, F., Duncan, C.A.J., Dupac, X., Ealet, A., Escoffier, S., Fabricius, M., Farina, M., Faustini, F., Ferriol, S., Finelli, F., Fotopoulou, S., Frailis, M., Franceschi, E., Galeotta, S., George, K., Gillis, B., Giocoli, C., Gómez-Alvarez, P., Gracia-Carpio, J., Granett, B.R., Grazian, A., Grupp, F., Gwyn, S., Haugan, S.V.H., Holmes, W., Hook, I.M., Hormuth, F., Hornstrup, A., Hudelot, P., Jahnke, K., Jhabvala, M., Joachimi, B., Keihänen, E., Kermiche, S., Kiessling, A., Kilbinger, M., Kubik, B., Kümmel, M., Kunz, M., Kurki-Suonio, H., Lahav, O., Le Boulc'h, Q., Le Brun, A.M.C., Le Mignant, D., Liebing, P., Ligori, S., Lilje, P.B., Lindholm, V., Lloro, I., Mainetti, G., Maino, D., Maiorano, E., Mansutti, O., Marcin, S., Marggraf, O., Martinelli, M., Martinet, N., Marulli, F., Massey, R., Maurogordato, S., McCracken, H.J., Medinaceli, E., Mei, S., Mellier, Y., Meneghetti, M., Merlin, E., Meylan, G., Mora, A., Moresco, M., Moscardini, L., Nakajima, R., Neissner, C., Niemi, S.-M., Nightingale, J.W., Padilla, C., Paltani, S., Pasian, F., Peacock, J.A., Pedersen, K., Percival, W.J., Pettorino, V., Pires, S., Polenta, G., Poncet, M., Popa, L.A., Pozzetti, L., Raison, F., Rebolo, R., Renzi, A., Rhodes, J., Riccio, G., Romelli, E., Roncarelli, M., Rusholme, B., Saglia, R., Sakr, Z., Sánchez, A.G., Sapone, D., Sartoris, B., Schewtschenko, J.A., Schirmer, M., Schneider, P., Schrabback, T., Scodeggio, M., Secroun, A., Seidel, G., Serrano, S., Simon, P., Sirignano, C., Sirri, G., Skottfelt, J., Stanco, L., Steinwagner, J., Tallada-Crespí, P., Tavagnacco, D., Taylor, A.N., Teplitz, H.I., Tereno, I., Tessore, N., Toft, S., Toledo-Moreo, R., Torradeflot, F., Tsyganov, A., Tutusaus, I., Valenziano, L., Valiviita, J., Vassallo, T., Verdoes Kleijn, G., Veropalumbo, A., Wang, Y., Weller, J., Zacchei, A., Zamorani, G., Zerbi, F.M., Zucca, E., Allevato, V., Ballardini, M., Bolzonella, M., Bozzo, E.: Euclid Quick Data Release (Q1). The role of cosmic connectivity in shaping galaxy clusters. arXiv e-prints, 2503–15332 (2025) https://doi.org/10.48550/arXiv.2503.15332 arXiv:2503.15332 [astro-ph.CO]

[25] Euclid Collaboration: Mellier, Y., Abdurro'uf, Acevedo Barroso, J.A., Achúcarro, A., Adamek, J., Adam, R., Addison, G.E., Aghanim, N., Aguena, M., Ajani, V., Akrami, Y., Al-Bahlawan, A., Alavi, A., Albuquerque, I.S., Alestas, G., Alguero, G., Allaoui, A., Allen, S.W., Allevato, V., Alonso-Tetilla, A.V., Altieri, B., Alvarez-Candal, A., Alvi, S., Amara, A., Amendola, L., Amiaux, J., Andika, I.T., Andreon, S., Andrews, A., Angora, G., Angulo, R.E., Annibali, F., Anselmi, A., Anselmi, S., Arcari, S., Archidiacono, M., Aricò, G., Arnaud, M., Arnouts, S., Asgari, M., Asorey, J., Atayde, L., Atek, H., Atrio-Barandela, F., Aubert, M., Aubourg, E., Auphan, T., Auricchio, N., Aussel, B., Aussel, H., Avelino, P.P., Avgoustidis, A., Avila, S., Awan, S., Azzollini, R., Baccigalupi, C., Bachelet, E.,

Bacon, D., Baes, M., Bagley, M.B., Bahr-Kalus, B., Balaguera-Antolinez, A., Balbinot, E., Balcells, M., Baldi, M., Baldry, I., Balestra, A., Ballardini, M., Ballester, O., Balogh, M., Bañados, E., Barbier, R., Bardelli, S., Baron, M., Barreiro, T., Barrena, R., Barriere, J.-C., Barros, B.J., Barthelemy, A., Bartolo, N., Basset, A., Battaglia, P., Battisti, A.J., Baugh, C.M., Baumont, L., Bazzanini, L., Beaulieu, J.-P., Beckmann, V., Belikov, A.N., Bel, J., Bellagamba, F., Bella, M., Bellini, E., Benabed, K., Bender, R., Benevento, G., Bennett, C.L., Benson, K., Bergamini, P., Bermejo-Climent, J.R., Bernardeau, F., Bertacca, D., Berthe, M., Berthier, J., Bethermin, M., Beutler, F., Bevillon, C., Bhargava, S., Bhatawdekar, R., Bianchi, D., Bisigello, L., Biviano, A., Blake, R.P., Blanchard, A., Blazek, J., Blot, L., Bosco, A., Bodendorf, C., Boenke, T., Böhringer, H., Boldrini, P., Bolzonella, M., Bonchi, A., Bonici, M., Bonino, D., Bonino, L., Bonvin, C., Bon, W., Booth, J.T., Borgani, S., Borlaff, A.S., Borsato, E., Bose, B., Botticella, M.T., Boucaud, A., Bouche, F., Boucher, J.S., Boutigny, D., Bouvard, T., Bouwens, R., Bouy, H., Bowler, R.A.A., Bozza, V., Bozzo, E., Branchini, E., Brando, G., Brau-Nogue, S., Brekke, P., Bremer, M.N., Brescia, M., Breton, M.-A., Brinchmann, J., Brinckmann, T., Brockley-Blatt, C., Brodwin, M., Brouard, L., Brown, M.L., Bruton, S., Bucko, J., Buddelmeijer, H., Buenadicha, G., Buitrago, F., Burger, P., Burigana, C., Busillo, V., Busonero, D., Cabanac, R., Cabayol-Garcia, L., Cagliari, M.S., Caillat, A., Caillat, L., Calabrese, M., Calabro, A., Calderone, G., Calura, F., Camacho Quevedo, B., Camera, S., Campos, L., Cañas-Herrera, G., Candini, G.P., Cantiello, M., Capobianco, V., Cappellaro, E., Cappelluti, N., Cappi, A., Caputi, K.I., Cara, C., Carbone, C., Cardone, V.F., Carella, E., Carlberg, R.G., Carle, M., Carminati, L., Caro, F., Carrasco, J.M., Carretero, J., Carrilho, P., Carron Duque, J., Carry, B.: Euclid: I. Overview of the Euclid mission. A&A **697**, 1 (2025) https://doi.org/10.1051/0004-6361/202450810 arXiv:2405.13491 [astro-ph.CO]

[26] Malavasi, N., Aghanim, N., Tanimura, H., Bonjean, V., Douspis, M.: Like a spider in its web: a study of the large-scale structure around the Coma cluster. A&A **634**, 30 (2020) https://doi.org/10.1051/0004-6361/201936629 arXiv:1910.11879 [astro-ph.CO]

[27] Einasto, M., Deshev, B., Tenjes, P., Heinämäki, P., Tempel, E., Juhan Liivamägi, L., Einasto, J., Lietzen, H., Tuvikene, T., Chon, G.: Multiscale cosmic web detachments, connectivity, and preprocessing in the supercluster SCl A2142 cocoon. A&A **641**, 172 (2020) https://doi.org/10.1051/0004-6361/202037982 arXiv:2007.04910 [astro-ph.CO]

[28] Castignani, G., Combes, F., Jablonka, P., Finn, R.A., Rudnick, G., Vulcani, B., Desai, V., Zaritsky, D., Salomé, P.: Virgo filaments. I. Processing of gas in cosmological filaments around the Virgo cluster. A&A **657**, 9 (2022) https://doi.org/10.1051/0004-6361/202040141 arXiv:2101.04389 [astro-ph.GA]

[29] Castignani, G., Vulcani, B., Finn, R.A., Combes, F., Jablonka, P., Rudnick, G., Zaritsky, D., Whalen, K., Conger, K., De Lucia, G., Desai, V., Koopmann,

R.A., Moustakas, J., Norman, D.J., Townsend, M.: Virgo Filaments. II. Catalog and First Results on the Effect of Filaments on Galaxy Properties. ApJs **259**(2), 43 (2022) https://doi.org/10.3847/1538-4365/ac45f7 arXiv:2110.13797 [astro-ph.GA]

[30] Malavasi, N., Sorce, J.G., Dolag, K., Aghanim, N.: The cosmic web around the Coma cluster from constrained cosmological simulations. I. Filaments connected to Coma at z = 0. A&A **675**, 76 (2023) https://doi.org/10.1051/0004-6361/202245777 arXiv:2306.03124 [astro-ph.CO]

[31] Aghanim, N., Tuominen, T., Bonjean, V., Gouin, C., Bonnaire, T., Einasto, M.: Dissecting a miniature universe: A multi-wavelength view of galaxy quenching in the Shapley supercluster. A&A **689**, 332 (2024) https://doi.org/10.1051/0004-6361/202348672 arXiv:2402.18455 [astro-ph.CO]

[32] Gouin, C., Bonnaire, T., Aghanim, N.: Shape and connectivity of groups and clusters: Effect of the dynamical state and accretion history. A&A **651**, 56 (2021) https://doi.org/10.1051/0004-6361/202140327 arXiv:2101.04686 [astro-ph.CO]

[33] Galárraga-Espinosa, D., Garaldi, E., Kauffmann, G.: Flows around galaxies. I. The dependence of galaxy connectivity on cosmic environments and effects on the star formation rate. A&A **671**, 160 (2023) https://doi.org/10.1051/0004-6361/202244935 arXiv:2209.05495 [astro-ph.GA]

[34] Santoni, S., De Petris, M., Yepes, G., Ferragamo, A., Bianconi, M., Gray, M.E., Kuchner, U., Pearce, F.R., Cui, W., Ettori, S.: THE THREE HUNDRED project: Estimating the dependence of gas filaments on the mass of galaxy clusters. A&A **692**, 44 (2024) https://doi.org/10.1051/0004-6361/202450895 arXiv:2405.17239 [astro-ph.CO]

[35] Bulbul, E., Liu, A., Kluge, M., Zhang, X., Sanders, J.S., Bahar, Y.E., Ghirardini, V., Artis, E., Seppi, R., Garrel, C., Ramos-Ceja, M.E., Comparat, J., Balzer, F., Böckmann, K., Brüggen, M., Clerc, N., Dennerl, K., Dolag, K., Freyberg, M., Grandis, S., Gruen, D., Kleinebreil, F., Krippendorf, S., Lamer, G., Merloni, A., Migkas, K., Nandra, K., Pacaud, F., Predehl, P., Reiprich, T.H., Schrabback, T., Veronica, A., Weller, J., Zelmer, S.: The SRG/eROSITA All-Sky Survey. The first catalog of galaxy clusters and groups in the Western Galactic Hemisphere. A&A **685**, 106 (2024) https://doi.org/10.1051/0004-6361/202348264 arXiv:2402.08452 [astro-ph.CO]

[36] Kluge, M., Comparat, J., Liu, A., Balzer, F., Bulbul, E., Ider Chitham, J., Ghirardini, V., Garrel, C., Bahar, Y.E., Artis, E., Bender, R., Clerc, N., Dwelly, T., Fabricius, M.H., Grandis, S., Hernández-Lang, D., Hill, G.J., Joshi, J., Lamer, G., Merloni, A., Nandra, K., Pacaud, F., Predehl, P., Ramos-Ceja, M.E., Reiprich, T.H., Salvato, M., Sanders, J.S., Schrabback, T., Seppi, R., Zelmer, S., Zenteno, A., Zhang, X.: The SRG/eROSITA All-Sky Survey. Optical identification and properties of galaxy clusters and groups in the western galactic hemisphere. A&A

**688**, 210 (2024) https://doi.org/10.1051/0004-6361/202349031 arXiv:2402.08453 [astro-ph.CO]

[37] Predehl, P., Andritschke, R., Arefiev, V., Babyshkin, V., Batanov, O., Becker, W., Böhringer, H., Bogomolov, A., Boller, T., Borm, K., Bornemann, W., Bräuninger, H., Brüggen, M., Brunner, H., Brusa, M., Bulbul, E., Buntov, M., Burwitz, V., Burkert, W., Clerc, N., Churazov, E., Coutinho, D., Dauser, T., Dennerl, K., Doroshenko, V., Eder, J., Emberger, V., Eraerds, T., Finoguenov, A., Freyberg, M., Friedrich, P., Friedrich, S., Fürmetz, M., Georgakakis, A., Gilfanov, M., Granato, S., Grossberger, C., Gueguen, A., Gureev, P., Haberl, F., Hälker, O., Hartner, G., Hasinger, G., Huber, H., Ji, L., Kienlin, A.v., Kink, W., Korotkov, F., Kreykenbohm, I., Lamer, G., Lomakin, I., Lapshov, I., Liu, T., Maitra, C., Meidinger, N., Menz, B., Merloni, A., Mernik, T., Mican, B., Mohr, J., Müller, S., Nandra, K., Nazarov, V., Pacaud, F., Pavlinsky, M., Perinati, E., Pfeffermann, E., Pietschner, D., Ramos-Ceja, M.E., Rau, A., Reiffers, J., Reiprich, T.H., Robrade, J., Salvato, M., Sanders, J., Santangelo, A., Sasaki, M., Scheuerle, H., Schmid, C., Schmitt, J., Schwope, A., Shirshakov, A., Steinmetz, M., Stewart, I., Strüder, L., Sunyaev, R., Tenzer, C., Tiedemann, L., Trümper, J., Voron, V., Weber, P., Wilms, J., Yaroshenko, V.: The eROSITA X-ray telescope on SRG. A&A **647**, 1 (2021) https://doi.org/10.1051/0004-6361/202039313 arXiv:2010.03477 [astro-ph.HE]

[38] Sunyaev, R., Arefiev, V., Babyshkin, V., Bogomolov, A., Borisov, K., Buntov, M., Brunner, H., Burenin, R., Churazov, E., Coutinho, D., Eder, J., Eismont, N., Freyberg, M., Gilfanov, M., Gureyev, P., Hasinger, G., Khabibullin, I., Kolmykov, V., Komovkin, S., Krivonos, R., Lapshov, I., Levin, V., Lomakin, I., Lutovinov, A., Medvedev, P., Merloni, A., Mernik, T., Mikhailov, E., Molodtsov, V., Mzhelsky, P., Müller, S., Nandra, K., Nazarov, V., Pavlinsky, M., Poghodin, A., Predehl, P., Robrade, J., Sazonov, S., Scheuerle, H., Shirshakov, A., Tkachenko, A., Voron, V.: SRG X-ray orbital observatory. Its telescopes and first scientific results. A&A **656**, 132 (2021) https://doi.org/10.1051/0004-6361/202141179 arXiv:2104.13267 [astro-ph.HE]

[39] Dey, A., Schlegel, D.J., Lang, D., Blum, R., Burleigh, K., Fan, X., Findlay, J.R., Finkbeiner, D., Herrera, D., Juneau, S., Landriau, M., Levi, M., McGreer, I., Meisner, A., Myers, A.D., Moustakas, J., Nugent, P., Patej, A., Schlafly, E.F., Walker, A.R., Valdes, F., Weaver, B.A., Yèche, C., Zou, H., Zhou, X., Abareshi, B., Abbott, T.M.C., Abolfathi, B., Aguilera, C., Alam, S., Allen, L., Alvarez, A., Annis, J., Ansarinejad, B., Aubert, M., Beechert, J., Bell, E.F., BenZvi, S.Y., Beutler, F., Bielby, R.M., Bolton, A.S., Briceño, C., Buckley-Geer, E.J., Butler, K., Calamida, A., Carlberg, R.G., Carter, P., Casas, R., Castander, F.J., Choi, Y., Comparat, J., Cukanovaite, E., Delubac, T., DeVries, K., Dey, S., Dhungana, G., Dickinson, M., Ding, Z., Donaldson, J.B., Duan, Y., Duckworth, C.J., Eftekharzadeh, S., Eisenstein, D.J., Etourneau, T., Fagrelius, P.A., Farihi, J., Fitzpatrick, M., Font-Ribera, A., Fulmer, L., Gänsicke, B.T., Gaztanaga, E., George, K., Gerdes, D.W., Gontcho, S.G.A., Gorgoni, C., Green, G., Guy,

J., Harmer, D., Hernandez, M., Honscheid, K., Huang, L.W., James, D.J., Jannuzi, B.T., Jiang, L., Joyce, R., Karcher, A., Karkar, S., Kehoe, R., Kneib, J.-P., Kueter-Young, A., Lan, T.-W., Lauer, T.R., Le Guillou, L., Le Van Suu, A., Lee, J.H., Lesser, M., Perreault Levasseur, L., Li, T.S., Mann, J.L., Marshall, R., Martínez-Vázquez, C.E., Martini, P., du Mas des Bourboux, H., McManus, S., Meier, T.G., Ménard, B., Metcalfe, N., Muñoz-Gutiérrez, A., Najita, J., Napier, K., Narayan, G., Newman, J.A., Nie, J., Nord, B., Norman, D.J., Olsen, K.A.G., Paat, A., Palanque-Delabrouille, N., Peng, X., Poppett, C.L., Poremba, M.R., Prakash, A., Rabinowitz, D., Raichoor, A., Rezaie, M., Robertson, A.N., Roe, N.A., Ross, A.J., Ross, N.P., Rudnick, G., Safonova, S., Saha, A., Sánchez, F.J., Savary, E., Schweiker, H., Scott, A., Seo, H.-J., Shan, H., Silva, D.R., Slepian, Z., Soto, C., Sprayberry, D., Staten, R., Stillman, C.M., Stupak, R.J., Summers, D.L., Sien Tie, S., Tirado, H., Vargas-Magaña, M., Vivas, A.K., Wechsler, R.H., Williams, D., Yang, J., Yang, Q., Yapici, T., Zaritsky, D., Zenteno, A., Zhang, K., Zhang, T., Zhou, R., Zhou, Z.: Overview of the DESI Legacy Imaging Surveys. AJ **157**(5), 168 (2019) https://doi.org/10.3847/1538-3881/ab089d arXiv:1804.08657 [astro-ph.IM]

[40] Zhou, R., Newman, J.A., Mao, Y.-Y., Meisner, A., Moustakas, J., Myers, A.D., Prakash, A., Zentner, A.R., Brooks, D., Duan, Y., Landriau, M., Levi, M.E., Prada, F., Tarle, G.: The clustering of DESI-like luminous red galaxies using photometric redshifts. MNRAS **501**(3), 3309–3331 (2021) https://doi.org/10.1093/mnras/staa3764 arXiv:2001.06018 [astro-ph.CO]

[41] Galárraga-Espinosa, D., Cadiou, C., Gouin, C., White, S.D.M., Springel, V., Pakmor, R., Hadzhiyska, B., Bose, S., Ferlito, F., Hernquist, L., Kannan, R., Barrera, M., Maria Delgado, A., Hernández-Aguayo, C.: Evolution of cosmic filaments in the MTNG simulation. A&A **684**, 63 (2024) https://doi.org/10.1051/0004-6361/202347982 arXiv:2309.08659 [astro-ph.CO]

[42] Aragón-Calvo, M.A., van de Weygaert, R., Jones, B.J.T.: Multiscale phenomenology of the cosmic web. MNRAS **408**(4), 2163–2187 (2010) https://doi.org/10.1111/j.1365-2966.2010.17263.x arXiv:1007.0742 [astro-ph.CO]

[43] Gallo, S., Aghanim, N., Gouin, C., Eckert, D., Douspis, M., Paste, J., Bonnaire, T.: Tracing gaseous filaments connected to galaxy clusters: The case study of Abell 2744. A&A **692**, 200 (2024) https://doi.org/10.1051/0004-6361/202451163 arXiv:2407.10518 [astro-ph.CO]

[44] Codis, S., Pichon, C., Pogosyan, D., Bernardeau, F., Matsubara, T.: Non-Gaussian Minkowski functionals and extrema counts in redshift space. MNRAS **435**(1), 531–564 (2013) https://doi.org/10.1093/mnras/stt1316 arXiv:1305.7402 [astro-ph.CO]

[45] Boldrini, P., Laigle, C.: Distinguishing dark matter theories with the cosmic web and next-generation surveys: I. An alternative theory of gravity. A&A

**700**, 182 (2025) https://doi.org/10.1051/0004-6361/202452238 arXiv:2402.04837 [astro-ph.CO]

[46] Mainieri, V., Anderson, R.I., Brinchmann, J., Cimatti, A., Ellis, R.S., Hill, V., Kneib, J.-P., McLeod, A.F., Opitom, C., Roth, M.M., Sanchez-Saez, P., Smiljanic, R., Tolstoy, E., Bacon, R., Randich, S., Adamo, A., Annibali, F., Arevalo, P., Audard, M., Barsanti, S., Battaglia, G., Bayo Aran, A.M., Belfiore, F., Bellazzini, M., Bellini, E., Beltran, M.T., Berni, L., Bianchi, S., Biazzo, K., Bisero, S., Bisogni, S., Bland-Hawthorn, J., Blondin, S., Bodensteiner, J., Boffin, H.M.J., Bonito, R., Bono, G., Bouche, N.F., Bowman, D., Braga, V.F., Bragaglia, A., Branchesi, M., Brucalassi, A., Bryant, J.J., Bryson, I., Busa, I., Camera, S., Carbone, C., Casali, G., Casali, M., Casasola, V., Castro, N., Catelan, M., Cavallo, L., Chiappini, C., Cioni, M.-R., Colless, M., Colzi, L., Contarini, S., Couch, W., D'Ammando, F., d'Assignies D., W., D'Orazi, V., da Silva, R., Dainotti, M.G., Damiani, F., Danielski, C., De Cia, A., de Jong, R.S., Dhawan, S., Dierickx, P., Driver, S.P., Dupletsa, U., Escoffier, S., Escorza, A., Fabrizio, M., Fiorentino, G., Fontana, A., Fontani, F., Forero Sanchez, D., Franois, P., Galindo-Guil, F.J., Gallazzi, A.R., Galli, D., Garcia, M., Garcia-Rojas, J., Garilli, B., Grand, R., Guarcello, M.G., Hazra, N., Helmi, A., Herrero, A., Iglesias, D., Ilic, D., Irsic, V., Ivanov, V.D., Izzo, L., Jablonka, P., Joachimi, B., Kakkad, D., Kamann, S., Koposov, S., Kordopatis, G., Kovacevic, A.B., Kraljic, K., Kuncarayakti, H., Kwon, Y., La Forgia, F., Lahav, O., Laigle, C., Lazzarin, M., Leaman, R., Leclercq, F., Lee, K.-G., Lee, D., Lehnert, M.D., Lira, P., Loffredo, E., Lucatello, S., Magrini, L., Maguire, K., Mahler, G., Zahra Majidi, F., Malavasi, N., Mannucci, F., Marconi, M., Martin, N., Marulli, F., Massari, D., Matsuno, T., Mattheee, J., McGee, S., Merc, J., Merle, T., Miglio, A., Migliorini, A., Minchev, I., Minniti, D., Miret-Roig, N., Monreal Ibero, A., Montano, F., Montet, B.T., Moresco, M., Moretti, C., Moscardini, L., Moya, A., Mueller, O., Nanayakkara, T., Nicholl, M., Nordlander, T., Onori, F., Padovani, M., Pala, A.F., Panda, S., Pandey-Pommier, M., Pasquini, L., Pawlak, M., Pessi, P.J., Pisani, A., Popovic, L.C., Prisinzano, L., Raddi, R., Rainer, M., Rebassa-Mansergas, A., Richard, J., Rigault, M., Rocher, A., Romano, D., Rosati, P., Sacco, G., Sanchez-Janssen, R., Sander, A.A.C., Sanders, J.L., Sargent, M., Sarpa, E., Schimd, C., Schipani, P., Sefusatti, E., Smith, G.P., Spina, L., Steinmetz, M., Tacchella, S., Tautvaisiene, G., Theissen, C., Thomas, G., Ting, Y.-S., Travouillon, T., Tresse, L., Trivedi, O., Tsantaki, M., Tsedrik, M., Urrutia, T., Valenti, E., Van der Swaelmen, M., Van Eck, S., Verdiani, F., Verdier, A., Vergani, S.D., Verhamme, A., Vernet, J., Verza, G., Viel, M., Vielzeuf, P., Vietri, G., Vink, J.S., Viscasillas Vazquez, C., Wang, H.-F., Weilbacher, P.M., Wendt, M., Wright, N., Ye, Q., Yeche, C., Yu, J., Zafar, T., Zibetti, S., Ziegler, B., Zinchenko, I.: The Wide-field Spectroscopic Telescope (WST) Science White Paper. arXiv e-prints, 2403–05398 (2024) https://doi.org/10.48550/arXiv.2403.05398 arXiv:2403.05398 [astro-ph.IM]

[47] Sousbie, T.: The persistent cosmic web and its filamentary structure - I. Theory and implementation. MNRAS **414**(1), 350–383 (2011) https://doi.org/10.1111/j.1365-2966.2011.18394.x arXiv:1009.4015 [astro-ph.CO]

[48] Sousbie, T., Pichon, C., Kawahara, H.: The persistent cosmic web and its filamentary structure - II. Illustrations. MNRAS **414**(1), 384–403 (2011) https://doi.org/10.1111/j.1365-2966.2011.18395.x arXiv:1009.4014 [astro-ph.CO]

[49] Cadiou, C., Pichon, C., Codis, S., Musso, M., Pogosyan, D., Dubois, Y., Cardoso, J.-F., Prunet, S.: When do cosmic peaks, filaments, or walls merge? A theory of critical events in a multiscale landscape. MNRAS **496**(4), 4787–4821 (2020) https://doi.org/10.1093/mnras/staa1853 arXiv:2003.04413 [astro-ph.CO]

[50] Malavasi, N., Aghanim, N., Douspis, M., Tanimura, H., Bonjean, V.: Characterising filaments in the SDSS volume from the galaxy distribution. A&A **642**, 19 (2020) https://doi.org/10.1051/0004-6361/202037647 arXiv:2002.01486 [astro-ph.CO]

[51] Driver, S.P., Norberg, P., Baldry, I.K., Bamford, S.P., Hopkins, A.M., Liske, J., Loveday, J., Peacock, J.A., Hill, D.T., Kelvin, L.S., Robotham, A.S.G., Cross, N.J.G., Parkinson, H.R., Prescott, M., Conselice, C.J., Dunne, L., Brough, S., Jones, H., Sharp, R.G., van Kampen, E., Oliver, S., Roseboom, I.G., Bland-Hawthorn, J., Croom, S.M., Ellis, S., Cameron, E., Cole, S., Frenk, C.S., Couch, W.J., Graham, A.W., Proctor, R., De Propris, R., Doyle, I.F., Edmondson, E.M., Nichol, R.C., Thomas, D., Eales, S.A., Jarvis, M.J., Kuijken, K., Lahav, O., Madore, B.F., Seibert, M., Meyer, M.J., Staveley-Smith, L., Phillipps, S., Popescu, C.C., Sansom, A.E., Sutherland, W.J., Tuffs, R.J., Warren, S.J.: GAMA: towards a physical understanding of galaxy formation. Astronomy and Geophysics **50**(5), 5–12519 (2009) https://doi.org/10.1111/j.1468-4004.2009.50512.x arXiv:0910.5123 [astro-ph.CO]

[52] Driver, S.P., Bellstedt, S., Robotham, A.S.G., Baldry, I.K., Davies, L.J., Liske, J., Obreschkow, D., Taylor, E.N., Wright, A.H., Alpaslan, M., Bamford, S.P., Bauer, A.E., Bland-Hawthorn, J., Bilicki, M., Bravo, M., Brough, S., Casura, S., Cluver, M.E., Colless, M., Conselice, C.J., Croom, S.M., de Jong, J., D'Eugenio, F., De Propris, R., Dogruel, B., Drinkwater, M.J., Dvornik, A., Farrow, D.J., Frenk, C.S., Giblin, B., Graham, A.W., Grootes, M.W., Gunawardhana, M.L.P., Hashemizadeh, A., Häußler, B., Heymans, C., Hildebrandt, H., Holwerda, B.W., Hopkins, A.M., Jarrett, T.H., Heath Jones, D., Kelvin, L.S., Koushan, S., Kuijken, K., Lara-López, M.A., Lange, R., López-Sánchez, Á.R., Loveday, J., Mahajan, S., Meyer, M., Moffett, A.J., Napolitano, N.R., Norberg, P., Owers, M.S., Radovich, M., Raouf, M., Peacock, J.A., Phillipps, S., Pimbblet, K.A., Popescu, C., Said, K., Sansom, A.E., Seibert, M., Sutherland, W.J., Thorne, J.E., Tuffs, R.J., Turner, R., van der Wel, A., van Kampen, E., Wilkins, S.M.: Galaxy And Mass Assembly (GAMA): Data Release 4 and the z ¡ 0.1 total and z ¡ 0.08 morphological galaxy stellar mass functions. MNRAS **513**(1), 439–467 (2022) https://doi.org/10.1093/mnras/stac472 arXiv:2203.08539 [astro-ph.GA]

[53] Treyer, M., Kraljic, K., Arnouts, S., de la Torre, S., Pichon, C., Dubois, Y., Vibert, D., Milliard, B., Laigle, C., Seibert, M., Brown, M.J.I., Grootes, M.W.,

Wright, A.H., Liske, J., Lara-Lopez, M.A., Bland-Hawthorn, J.: Group quenching and galactic conformity at low redshift. MNRAS **477**(2), 2684–2704 (2018) https://doi.org/10.1093/mnras/sty769 arXiv:1712.05318 [astro-ph.GA]

[54] Kraljic, K., Arnouts, S., Pichon, C., Laigle, C., de la Torre, S., Vibert, D., Cadiou, C., Dubois, Y., Treyer, M., Schimd, C., Codis, S., de Lapparent, V., Devriendt, J., Hwang, H.S., Le Borgne, D., Malavasi, N., Milliard, B., Musso, M., Pogosyan, D., Alpaslan, M., Bland-Hawthorn, J., Wright, A.H.: Galaxy evolution in the metric of the cosmic web. MNRAS **474**(1), 547–571 (2018) https://doi.org/10.1093/mnras/stx2638 arXiv:1710.02676 [astro-ph.GA]

[55] Liu, A., Bulbul, E., Ghirardini, V., Liu, T., Klein, M., Clerc, N., Özsoy, Y., Ramos-Ceja, M.E., Pacaud, F., Comparat, J., Okabe, N., Bahar, Y.E., Biffi, V., Brunner, H., Brüggen, M., Buchner, J., Ider Chitham, J., Chiu, I., Dolag, K., Gatuzz, E., Gonzalez, J., Hoang, D.N., Lamer, G., Merloni, A., Nandra, K., Oguri, M., Ota, N., Predehl, P., Reiprich, T.H., Salvato, M., Schrabback, T., Sanders, J.S., Seppi, R., Thibaud, Q.: The eROSITA Final Equatorial-Depth Survey (eFEDS). Catalog of galaxy clusters and groups. A&A **661**, 2 (2022) https://doi.org/10.1051/0004-6361/202141120 arXiv:2106.14518 [astro-ph.CO]

[56] Klein, M., Oguri, M., Mohr, J.J., Grandis, S., Ghirardini, V., Liu, T., Liu, A., Bulbul, E., Wolf, J., Comparat, J., Ramos-Ceja, M.E., Buchner, J., Chiu, I., Clerc, N., Merloni, A., Miyatake, H., Miyazaki, S., Okabe, N., Ota, N., Pacaud, F., Salvato, M., Driver, S.P.: The eROSITA Final Equatorial-Depth Survey (eFEDS). Optical confirmation, redshifts, and properties of the cluster and group catalog. A&A **661**, 4 (2022) https://doi.org/10.1051/0004-6361/202141123 arXiv:2106.14519 [astro-ph.CO]

[57] Euclid Collaboration: Laigle, C., Gouin, C., Sarron, F., Quilley, L., Pichon, C., Kraljic, K., Durret, F., Chisari, N.E., Kuchner, U., Malavasi, N., Magliocchetti, M., McCracken, H.J., Sorce, J.G., Kang, Y., McPartland, C.J.R., Toft, S., Aghanim, N., Altieri, B., Amara, A., Andreon, S., Auricchio, N., Aussel, H., Baccigalupi, C., Baldi, M., Balestra, A., Bardelli, S., Basset, A., Battaglia, P., Bernardeau, F., Biviano, A., Bonchi, A., Branchini, E., Brescia, M., Brinchmann, J., Camera, S., Cañas-Herrera, G., Capobianco, V., Carbone, C., Carretero, J., Casas, S., Castellano, M., Castignani, G., Cavuoti, S., Chambers, K.C., Cimatti, A., Colodro-Conde, C., Congedo, G., Conselice, C.J., Conversi, L., Copin, Y., Courbin, F., Courtois, H.M., Cropper, M., Da Silva, A., Degaudenzi, H., de la Torre, S., De Lucia, G., Di Giorgio, A.M., Dolding, C., Dole, H., Dubath, F., Duncan, C.A.J., Dupac, X., Ealet, A., Escoffier, S., Farina, M., Farinelli, R., Faustini, F., Ferriol, S., Finelli, F., Fotopoulou, S., Frailis, M., Franceschi, E., Galeotta, S., George, K., Gillard, W., Gillis, B., Giocoli, C., Gómez-Alvarez, P., Gracia-Carpio, J., Granett, B.R., Grazian, A., Grupp, F., Gwyn, S., Haugan, S.V.H., Hoekstra, H., Holmes, W., Hook, I.M., Hormuth, F., Hornstrup, A., Hudelot, P., Jahnke, K., Jhabvala, M., Joachimi, B., Keihänen, E., Kermiche, S., Kiessling, A., Kilbinger, M., Kubik, B., Kuijken, K., Kümmel, M., Kunz, M., Kurki-Suonio,

H., Le Boulc'h, Q., Le Brun, A.M.C., Le Mignant, D., Liebing, P., Ligori, S., Lilje, P.B., Lindholm, V., Lloro, I., Mainetti, G., Maino, D., Maiorano, E., Mansutti, O., Marcin, S., Marggraf, O., Martinelli, M., Martinet, N., Marulli, F., Massey, R., Maurogordato, S., Medinaceli, E., Mei, S., Melchior, M., Mellier, Y., Meneghetti, M., Merlin, E., Meylan, G., Mora, A., Moresco, M., Moscardini, L., Nakajima, R., Neissner, C., Niemi, S.-M., Nightingale, J.W., Padilla, C., Paltani, S., Pasian, F., Pedersen, K., Percival, W.J., Pettorino, V., Pires, S., Polenta, G., Poncet, M., Popa, L.A., Pozzetti, L., Raison, F., Rebolo, R., Renzi, A., Rhodes, J., Riccio, G., Romelli, E., Roncarelli, M., Rusholme, B., Saglia, R., Sakr, Z., Sánchez, A.G., Sapone, D., Sartoris, B., Schewtschenko, J.A., Schirmer, M., Schneider, P., Schrabback, T., Scodeggio, M., Secroun, A., Seidel, G., Seiffert, M., Serrano, S., Simon, P., Sirignano, C., Sirri, G., Skottfelt, J., Stanco, L., Steinwagner, J., Tallada-Crespí, P., Taylor, A.N., Teplitz, H.I., Tereno, I., Tessore, N., Toledo-Moreo, R., Torradeflot, F., Tutusaus, I., Valenziano, L., Valiviita, J., Vassallo, T., Verdoes Kleijn, G., Veropalumbo, A., Wang, Y., Weller, J., Zacchei, A., Zamorani, G., Zerbi, F.M., Zinchenko, I.A., Zucca, E., Allevato, V., Ballardini, M., Bolzonella, M., Bozzo, E.: Euclid Quick Data Release (Q1). Galaxy shapes and alignments in the cosmic web. arXiv e-prints, 2503–15333 (2025) https://doi.org/10.48550/arXiv.2503.15333 arXiv:2503.15333 [astro-ph.GA]

[58] Einasto, M., Kipper, R., Tenjes, P., Lietzen, H., Tempel, E., Liivamägi, L.J., Einasto, J., Tamm, A., Heinämäki, P., Nurmi, P.: The Corona Borealis supercluster: connectivity, collapse, and evolution. A&A **649**, 51 (2021) https://doi.org/10.1051/0004-6361/202040200 arXiv:2103.02326 [astro-ph.CO]

[59] Kraljic, K., Pichon, C., Codis, S., Laigle, C., Davé, R., Dubois, Y., Hwang, H.S., Pogosyan, D., Arnouts, S., Devriendt, J., Musso, M., Peirani, S., Slyz, A., Treyer, M.: The impact of the connectivity of the cosmic web on the physical properties of galaxies at its nodes. MNRAS **491**(3), 4294–4309 (2020) https://doi.org/10.1093/mnras/stz3319 arXiv:1910.08066 [astro-ph.GA]

[60] Galárraga-Espinosa, D., Kauffmann, G., Bonoli, S., Lucie-Smith, L., González Delgado, R.M., Tempel, E., Abramo, R., Gurung-López, S., Marra, V., Alcaniz, J., Benitez, N., Carneiro, S., Cenarro, J., Cristóbal-Hornillos, D., Dupke, R., Ederoclite, A., Hernán-Caballero, A., Hernández-Monteagudo, C., López-Sanjuan, C., Marín-Franch, A., Mendes de Oliveira, C., Moles, M., Sodré, L. Jr., Taylor, K., Varela, J., Vázquez Ramió, H.: Unveiling the small-scale web around galaxies with miniJPAS and DESI. A&A **706**, 21 (2026) https://doi.org/10.1051/0004-6361/202556021 arXiv:2506.15345 [astro-ph.CO]